E-ELT PROGRAMME

MICADO Phase A
Single Conjugate Adaptive Optics Module

Document: E-TRE-MCD-561-0022

Issue: 1.0

Date: 22.10.09

	Name	Date & Signature
Author(s)	Y. Clénet P. Bernardi F. Chapron E. Gendron Z. Hubert G. Rousset	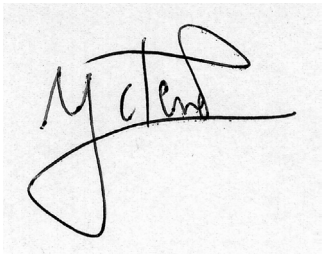
Proj. Manager	R. Davies	

CHANGE RECORD

ISSUE	DATE	SECTION/PAGE AFFECTED	REASON/ REMARKS
1	22/10/2009	All	First issue

TABLE OF CONTENTS

ABBREVIATIONS AND ACRONYMS

AO	adaptive optics
E-ELT	European Extremely Large Telescope
ESO	European Southern Observatory
FTE	Full Time Equivalent (year)
GLAO	ground layer adaptive optics
GMT	Giant Magellan Telescope
JWST	James Web Space Telescope
MAORY	McAO RelaY
MCAO	multiconjugate adaptive optics
MICADO	The Multi-AO Imaging Camera for Deep Observations
MPE	Max-Planck-Institut für extraterrestrische Physik
MPIA	Max-Planck-Institut für Astronomie
NOVA	Nederlandse Onderzoekschool voor Astronomie
OAPD	Osservatorio Astronomico di Padova
PSF	Point Spread Function
RTC	Real-Time Controller
SAMI	ScAo for MIcado
SCAO	single conjugated adaptive optics
TLR	Top-Level Requirements
TMT	Thirty Meter Telescope
USM	Universitäts-Sternwarte München
WFS	wave front sensor
WP	Workpackage

1 SCOPE

This document describes the opto-mechnical design of SAMI, the single conjugated adaptive optics module that would equip MICADO until MAORY is fully operational and available for MICADO. The document also provides estimated performance of this module.

2 APPLICABLE AND REFERENCE DOCUMENTS

2.1 Applicable Documents

The following applicable documents form a part of the present document to the extent specified herein. In the event of conflict between applicable documents and the content of the present document, the present document shall be taken as superseding.

AD1 Common definitions and acronyms, E-ESO-SPE-313-0066, Issue 1

AD2 E-ELT interfaces for scientific instruments, E-TRE-ESO-586-0252 Issue 2

AD3 Call for Proposal For a Phase A Study of a High Angular Resolution Camera for the E-ELT, Specifications of the Instrument to be studied, E-ESO-SPE-561-0097, v1.0

AD4 Statement of Work for the Phase A Design of MICADO, E-SOW-ESO-561-0127, v1.0

AD5 Guidelines for the post-focal SCAO NGS wavefront sensor for the E-ELT AO based instrumentation, E-TRE-ESO-528-0462, v0.4

AD6 E-ELT AO design inputs: relevant atmospheric parameters, E-SPE-ESO-276-0206 issue 1

AD7 Technical specifications for the conceptual design, prototyping, preliminary design of the M4 adaptive unit for the E-ELT, E-SPE-ESO-106-0037, issue 3

AD8 "EELT Optical Design Report", E-TRE-ESP-227-138, issue 3

AD9 ATLAS AO system analysis and performance, E-TRE-ONE-528-0020, version 1

AD10 Database of technical data for E-ELT simulations (www.eso.org/sci/facilities/eelt/science/drm/tech_data/)

AD11 MAORY Phase A study, Status at mid-term progress meeting, E-TRE-INA-528-0021 Issue 1

2.2 Reference Documents

RD1 MICADO Phase A Development and Management Plan, E-PLA-MCD-561-0020, v1.0

RD2 MICADO Scientific Analysis Report, E-TRE-MCD-561-0007, v 1.0

RD3 MICADO System Overview, E-TRE-MIC-561-0009, v 2.0

RD4 MICADO Design Trade-Off and Risk Assessment, E-TRE-MCD-561-0010, v 2.0

RD5 MICADO Opto-Mechanical Design and Analysis, E-TRE-MCD-561-0011, v 5.0

3 WHY AN SCAO MODULE FOR MICADO ?

MICADO, the MCAO Imaging Camera for Deep Observations, is being designed to work with adaptive optics on the E-ELT. The instrument is intended to image, through selected wide and narrow-band near infrared filters, a wide (about 60") field of view at the diffraction limit of the E-ELT. It is primarily intended to work with the multi-conjugate AO system MAORY. Though, MAORY is not expected to be fully operational and available for MICADO at the first light of MICADO. Till then, the SCAO module will deliver on-axis diffraction-limited images to MICADO allowing one to fulfil some of the MICADO science cases.

4 SCAO MODULE TOP-LEVEL REQUIREMENTS

The SCAO module being not part of the original ESO call for proposal, the top-level requirements adopted for the MICADO SCAO module were established with the goal to adopt as much as possible the same interfaces with MICADO as the ones MICADO has with MAORY. The SCAO TLR were also established having in mind that the SCAO module will be used only during the first years of MICADO operations and could consequently work with restrained specifications (e.g., field of view).

TLR #	TLR	TLR value	Comments
SCAO_TLR1	Patrol field of view	45"	Diameter
SCAO_TLR2	WFS bandpass	0.45-0.8 μm	
SCAO_TLR3	Repositioning accuracy for small dither	2 mas	Offset value: ±0.3 mas Offset timescale: few tenths of second (TBC) AO loop closed between offsetting The offset is done by AO
SCAO_TLR4	Repositioning accuracy for large dither	2 mas	Offset value: few seconds Offset timescale: up to 30 sec (TBC) AO loop closed on both offset positions, opened during offsetting The offset is done by the telescope
SCAO_TLR5	Relay optics image quality	80% @ 0.8μm	
SCAO_TLR6	Relay optics magnification	1	As for MAORY
SCAO_TLR7	SCAO module transmission	80%	At infrared wavelengths

SCAO_TLR8	SCAO module above MICADO, in a gravity invariant position		

Table 1: SCAO module top-level requirements

One should note in this top-level requirements that we have been asked to study a visible wavefront sensor. Though, in conjunction with science case priorities, this choice could be revisited in Phase B to study the implementation of an infrared wavefront sensor or both an infrared and a visible wavefront sensor.

5 SAMI DESIGN OVERVIEW

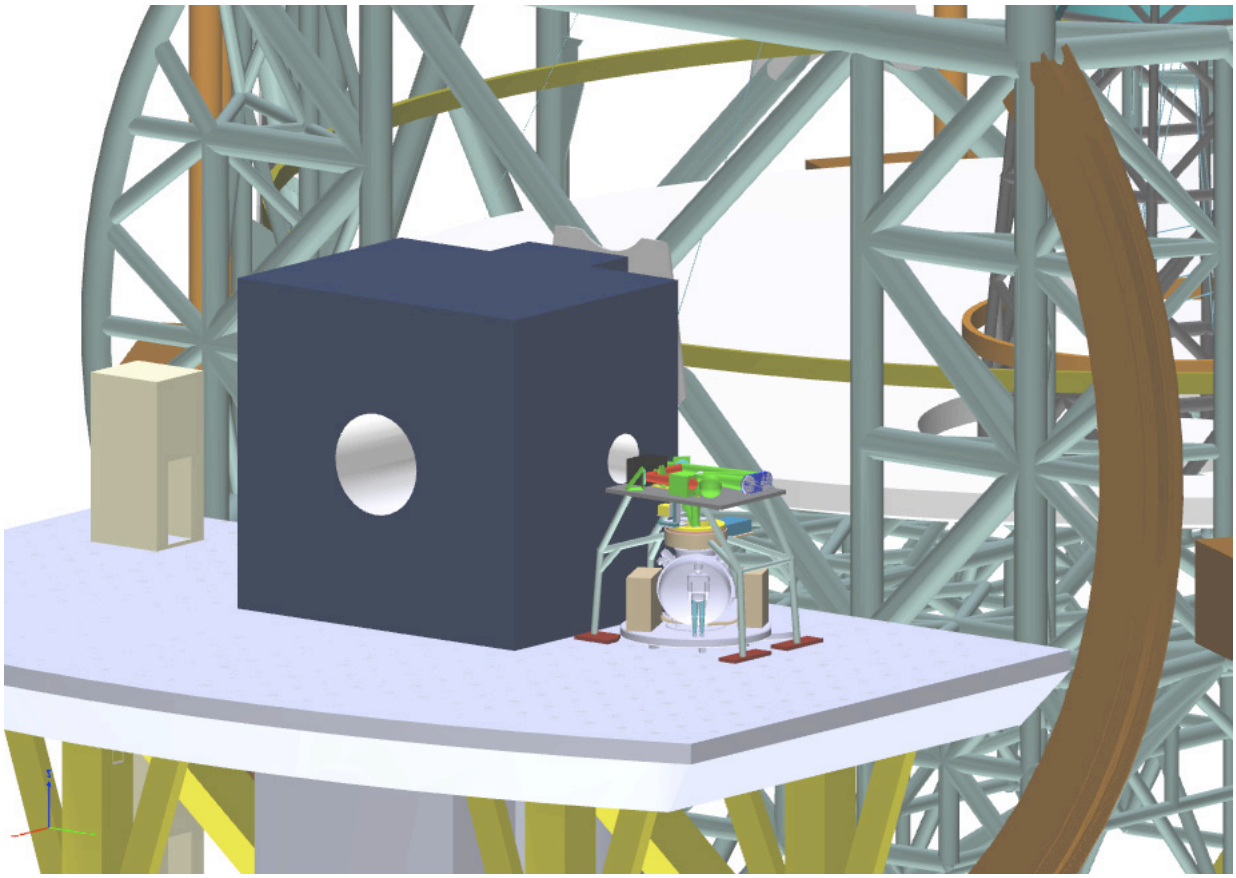

Figure 1: General view of MICADO and SAMI mounted on the E-ELT Nasmyth platform.

SAMI aims at providing a corrected beam to MICADO until MAORY is available for that purpose. Hence, SAMI will occupy the future MAORY location, above MICADO. SAMI will actually ensure four functionalities, each of them corresponding to a dedicated subsystem:

- provide an optical relay between the telescope beam and MICADO,
- derotate the field while the telescope tracks the scientific target,
- deliver to MICADO an adaptive optics corrected beam thanks to a dedicated WFS,
- support the MICADO cryostat on the E-ELT Nasmyth platform.

In the following, we briefly describe each of these subsystems.

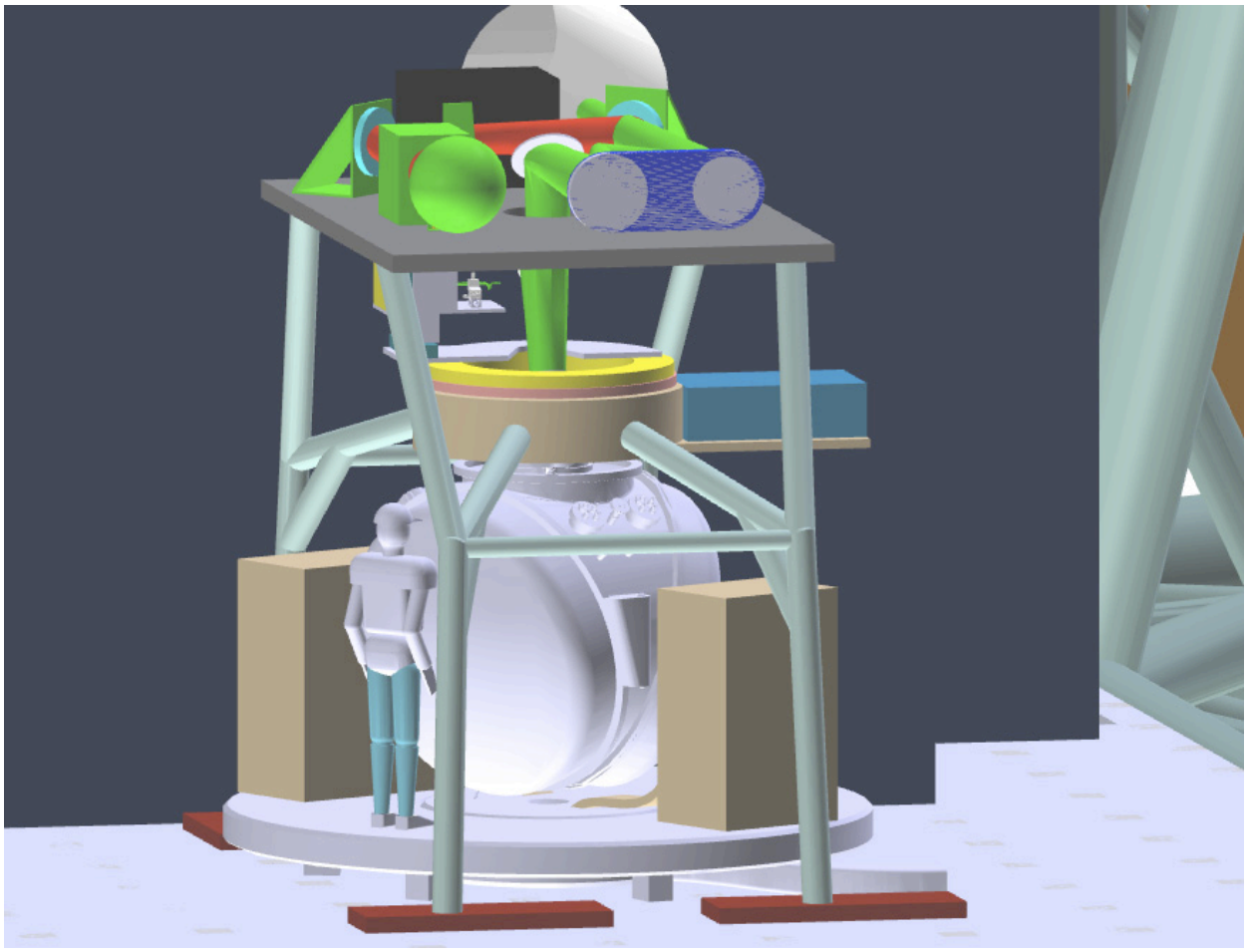

Figure 2: Closer view of MICADO and SAMI, with their support structure. The upper table is the relay optics bench supporting the relay optics and the MICADO calibration unit. The yellow+rose cylinders are the derotator. The blue box is the derotator motor. At the left of the green vertical optical beam, one can guess the WFS on its movable support. The brown parts at the bottom of the arch-like support structure are the interfaces with the Nasmyth platform

5.1 The relay optics

Given the too small back focal distance of the E-ELT (750 mm, cf. AD2), an optical relay has to be included into the beam between the E-ELT flange and the MICADO focal plane. This relay is made of

- a 3-mirror Offner relay (M7, M8 and M9), mounted and fixed on an optical bench,
- a folding mirror (M10) that direct the beam downward (SCAO_TLR8) to the dichroic plate and MICADO,
- a dichroic plate, reflecting the light between 0.45 and 0.8 µm towards the WFS and transmiting the light between 0.8 and 2.32 µm towards MICADO (SCAO_TLR2).

A magnification of 1, similar to MAORY's one, has been adopted (SCAO_TLR6) leading to a scale of 3.605 mm/arcsec.

A summary of the optical performances of the relay optics is given in the following table.

Parameters	Goal	Value
Field of View	45''	45''
F/#	17.71	17.71
Scale	3.605 mm/ 1''	3.603 mm/ 1''
Field curvature	1.3m from MAORY, 43.8m from ELT	∞
Image quality	Strehl ratio better than 80% @ 0.8 µm	> 80% @ 0.8µm
Exit pupil location	∞ from MAORY, -43.3m from ELT	+77m
Back focal distance	500 mm	667.2 mm
Transmitted wavelength range	0.8 – 2.32 µm	0.8 – 2.32 µm

Table 2: Relay optics performances

Details on the optical and mechanical designs can be found in Section 6 and 7, respectively.

5.2 The derotator and support structure

MICADO being located at the E-ELT Nasmyth platform, a field derotator has to be provided to MICADO to compensate for the telescope movements. We assume a specification of the derotator to be able to rotate of 360° in about 20 min.

The dichroic plate, M11, the wavefront sensor and MICADO are rotating together with the derotator.

This derotator is included in a support structure. This structure supports both MICADO and the WFS assembly. The next figure shows are general view of MICADO on the Nasmyth platform. Details on the support structure and derotator are found in Section 7.1.

5.3 M11 mirror

This mirror picks off the WFS beam light after the dichroic plate and sends it to the WFS. This mirror is used to ensure several functions:

- since M7 and M9 are spherical, the exit pupil of the relay optics is not at infinity, but at 77m, resulting in tilted images. This effect is corrected by tilting M11. The maximum tilt angle is given by the field size at 77m: 170 mm/77 mm = 0.126°. Hence to correct for the impact of the exit pupil location, M11 has to be tilted of a maximum angle of ±0.063°, in rather large timescales (minutes),
- one has to correct for the E-ELT pupil run out. We assume this run out to be 1% of its diameter (a run out value for the Coudé focus is given in AD2 but non for the Nasmyth

focus, hence we assumed the same value as for the Coudé focus), which translates into 1/1771 = 0.034°. This run out is assumed to be very slow, on minute timescales,

- one has to correct the WFS K-mirror misalignment effects when this K-mirror rotates. We assumed a maximum tilt angle of ±1°.

Hence, the maximum tilt angle must be ±1°. The accuracy of these tilt corrections must be about 1/1000 of the pupil size, i.e. 1/17710= 3.24e-3 degrees.

5.4 The wavefront sensor

5.4.1 Overview

The concept of this wavefront sensor follows the guidelines of AD5: it is a Shack-Hartmann wavefront sensor and it assumes the same camera and detector. Hence, the dimensions of this camera are width 340 mm × height 240 mm × depth 300 mm and its weight is 10 kg. The detector readout noise is assumed to be 3 e^- and its quantum efficiency 85% on the WFS bandpass (0.45-0.8 microns).

The WFS includes a field stop, a K-mirror, a lens triplet, the micro-lenses and the camera. To pick-off the AO reference star, this whole assembly can move along X and Y directions in front of the M11 mirror. The total amplitude of these displacements, to cover the 45" field (SCAO_TLR1), is ± 85 mm.

The jitter specifications translate into

- SCAO_TLR3: a displacement of the WFS of ±1.08 mm in a fraction of second with a repositioning accuracy of 7 microns,
- SCAO_TLR4: a displacement of the WFS of ±18 mm in less than 30 seconds with a repositioning accuracy of 7 microns.

The K-mirror function is to rotate the pupil of the WFS (see Section 5.4.2). We assume the mirrors to be mounted in a single assembly. The K-mirror will rotate at the same speed as the derotator, but in the opposite direction, hence a specification to be able to rotate of 360° in about 20 minutes.

5.4.2 Pupil and field rotation

In our baseline, we have chosen to have the WFS rotating together with M4, to ensure a proper conjugation of the microlenses with the M4 actuators. The alternative would have been to let the microlenses rotate with respect to M4 and to update in real time the AO control matrix. The latter solution has not been chosen since not considered as a mature technique and then too risky for MICADO regarding the will to adopt confirmed solutions.

Having the dichroic plate rotating also together with the WFS, we hence have the WFS, the dichroic plate and MICADO rotating together with the field. It implies to mount the WFS on a x/y stage for the reference source pick-off and the offsets/dithers and to include in the WFS a pupil rotation stage (the K-mirror). The alternative to this K-mirror would have been to rotate the whole WFS assembly together with the pupil but, once again, we have considered it as a too complex solution, given the possible rotation amplitude.

5.4.3 ADC

We study in this section the need, or not, for such an ADC in the WFS.

The variation of the refraction index with respect to the wavelength induces a shift of the WFS spot with respect to the wavelength. This effect is modulated by the effective flux received from the reference source with respect to the wavelength, i.e. by the detector quantum efficiency and the reference source spectrum. It thus leads to an enlarged spot size if no atmospheric dispersion corrector is inserted inside the WFS beam.

5.4.3.1 Atmospheric dispersion model

The atmospheric dispersion, in arcsec, is given by:

$$\Delta R(\lambda, \lambda_0, z) = 206264.8\,(n(\lambda) - n(\lambda_0))\tan z$$

where $n(\lambda)$ is the air refractive index at wavelength λ (expressed in microns), λ_0 is the reference wavelength and z is the considered zenith distance. From Owens (1967, Applied Optics, vol 6, n°1, p51-59):

$$\begin{aligned}(n(\lambda)-1)\,10^8 &= \left(2371.34 + \frac{683939.7}{130-\lambda^{-2}} + \frac{4547.3}{38.9-\lambda^{-2}}\right) D_1 \\ &\quad + \left(6487.31 + 58.058\,\lambda^{-2} - 0.7115\,\lambda^{-4} + 0.08851\,\lambda^{-6}\right) D_2\end{aligned}$$

with

$$D_1 = \frac{P_1}{T}\left(1 + P_1\left(57.90\times10^{-8} - \frac{9.325\times10^{-4}}{T} + \frac{0.25844}{T^2}\right)\right)$$

$$D_2 = \frac{P_2}{T}\left(1 + P_2\left(1 + 3.7\times10^{-4}P_2\right)\left(-2.37321\times10^{-3} + \frac{2.23366}{T} - \frac{710.792}{T^2} + \frac{7.75141\times10^4}{T^3}\right)\right)$$

where T, R_H and P are the considered temperature (in Kelvins), relative humidity (in %) and pressure (in mbar) for the observing site, and

$$P_2 = \frac{R_H \times P_S}{100} \qquad P_1 = P - P_2$$

$$P_S = -10474.0 + 116.43\times T - 0.43284\times T^2 + 0.00053840\times T^3$$

In the following, we use the typical Paranal atmospheric conditions (http://www.eso.org/gen-fac/pubs/astclim/lasilla/diffrefr.html): T=284.65 K, R_H=14.5% and P=743 mbar.

5.4.3.2 Effective flux on the WFS detector

The flux vs. wavelength is given by the WFS reference source spectrum multiplied by the detector quantum efficiency and by the WFS band-pass.

5.4.3.2.1 WFS reference source spectrum

As a reference source spectrum, we consider the Planck law *PL(λ,T)* of the black body whose temperature is the typical effective temperature of the reference source spectral type. More than 90% of stars are M stars with T_{eff} between 2800 and 3800 K.

5.4.3.2.2 Detector quantum efficiency

The detector we consider here is based on the feasibility studies launched by ESO for large, fast low noise, visible detector for AO wavefront sensing (AD5). The technology adopted by contractors for a Technology Demonstrator is based on CMOS. The expected quantum efficiency for these detectors is given in the figure below (J. Kolb, private communication).

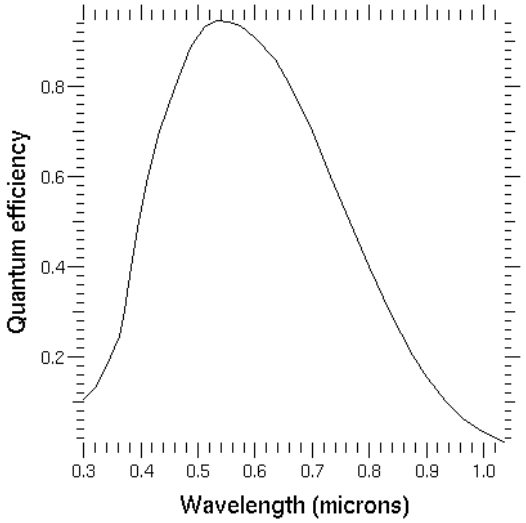

Figure 3: Considered detector quantum efficiency

5.4.3.2.3 WFS bandpass

We simply consider a window function $W(\lambda,\lambda_{inf},\lambda_{sup})$ as the transmission curve, with 1 between the shortest and largest cut-off wavelength and 0 outside. MICADO needing to observe down to 0.8 microns, we consider the latter value as the WFS largest cut-off wavelength λ_{sup}. In the following, the WFS shortest cut-off frequency λ_{inf} will be varied to study the effect of the WFS band-pass on the WFS spot size without ADC.

5.4.3.2.4 Flux dispersion

Let's consider *F(p)* the flux received on the detector as a function of the position *p* on the detector and $\phi(\lambda)$ the flux received on the detector as a function of the wavelength. The flux conservation leads to

$$F(p)\,dp = \phi(\lambda)\,d\lambda$$

$$F(p) = \frac{\phi(\lambda)}{dp/d\lambda} = \frac{PL(\lambda, T_{eff}) \times QE(\lambda) \times W(\lambda, \lambda_{inf}, \lambda_{sup})}{d\Delta R(\lambda, \lambda_0, z)/d\lambda}$$

The FWHM *ΔG* of the monochromatic spot function *G(p,ΔG)* has been computed with an home-made simulation tool of an AO loop for a single Shack-Hartmann subaperture (see Section 10.7.1.1). The next figure shows the values of *ΔG* for different wavelengths and zenith angles, computed with the SCAO dimensioning atmospheric parameters of AD6 (see also Section 10.1).

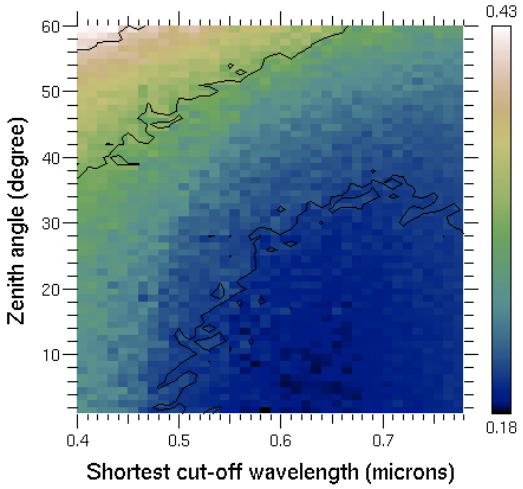

Figure 4: WFS monochromatic spot FWHM *ΔG*, in arcsec Contours, for bottom right to top left are for 0.2", 0.3" and 0.4"

The polychromatic spot flux *f(p)* is the given by the convolution of *F(p)* with *G(p, ΔG)*:

$$f = FFT^{-1}(FFT(F) \times \overline{FFT(G)})$$

We can then evaluate the FWHM *Δf* of the polychromatic spot flux function *f(p)* as a function of the shortest cut-off wavelength of the WFS bandpass.

Hence, for typical M stars of the main sequence, the atmospheric dispersion enlarges the WFS spot up to ~0.3" for the design conditions at a zenith angle of 30°.

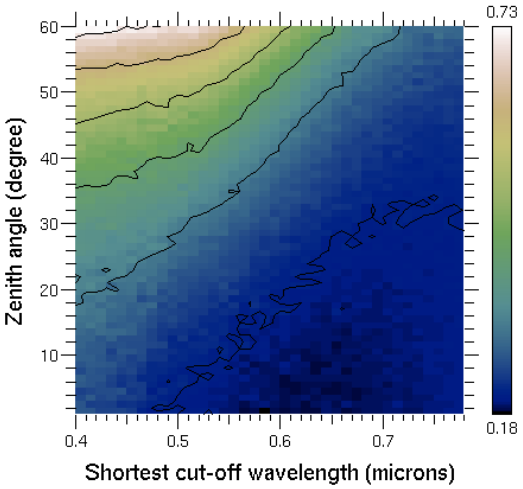

Figure 5: WFS polychromatic spot FWHM *Δf*, in arcsec, when no ADC is used and for a effective reference source temperature of 3300 K, as a function of the shortest WFS cut-off wavelength and of the zenith angle. Contours are for 0.2", 0.3", 0.4", 0.5", 0.6", 0.7", from bottom to top

5.4.3.2.5 WFS noise

In the photon noise regime, the WFS noise σ^2 is proportional to $\theta_b^2/np(\lambda_{inf},\lambda_{sup})$ where θ_b is the size of the blurred WFS spot and $np(\lambda_{inf},\lambda_{sup})$ is the number of photons per subaperture and per frame within the $(\lambda_{inf},\lambda_{sup})$ band-pass. Hence, the noise, $\sigma_0(z, 0.45)$ when using an ADC, at a given zenith angle z and for the entire WFS bandpass [0.45 μm, 0.8 μm] is given by:

$$\sigma_0^2(z, 0.45) = \frac{f^2(z, 0.45)}{np_{w/ADC}(0.45)}$$

And the noise, when not using any ADC, at a given zenith angle z and for a WFS bandpass [λ_{min}, 0.8 μm] is given by:

$$\sigma_{w/o\,ADC}^2(z, \lambda_{min}) = \frac{f^2(z, \lambda_{min}) + \Delta G^2(z, \lambda_{min})}{2 \times np_{w/o\,ADC}(\lambda_{min})}$$

This expression takes into account a WFS spot elongation by the atmospheric dispersion along only one direction and then separates the WFS noise into different x and y components.

The latter expression can be converted into a equivalent noise with an ADC $\sigma_{0\,eq}(z, 0.45)$ using a reducing factor α, which then represents a normalised equivalent number of photons:

$$\sigma_{0\,eq}^2(z, 0.45) = \frac{f^2(z, 0.45)}{np_{w/ADC}(0.45) \times \alpha}$$

The magnitude loss expression is then:

$$-2.5 \log \left(\frac{2 \times f^2(z, 0.45)}{f^2(z, 0.45) + \Delta G^2(z, 0.45)} \frac{np_{w/oADC}(\lambda_{min})}{np_{w/ADC}(0.45)} \right)$$

With the number of photons without and with ADC ratio equal to:

$$\frac{np_{w/oADC}(\lambda_{min})}{np_{w/ADC}(0.45)} = \frac{\int_{\lambda_{inf}}^{0.8} PL(\lambda, T_{eff}) \times QE(\lambda)\, d\lambda}{\int_{0.45}^{0.8} PL(\lambda, T_{eff}) \times QE(\lambda) \times t_{ADC}(\lambda)\, d\lambda}$$

where $t_{ADC}(\lambda)$ is the ADC transmission, assumed to be 0.8.

The following figure shows the magnitude loss when not using any ADC as a function of the shortest cut-off wavelength of the WFS bandpass.

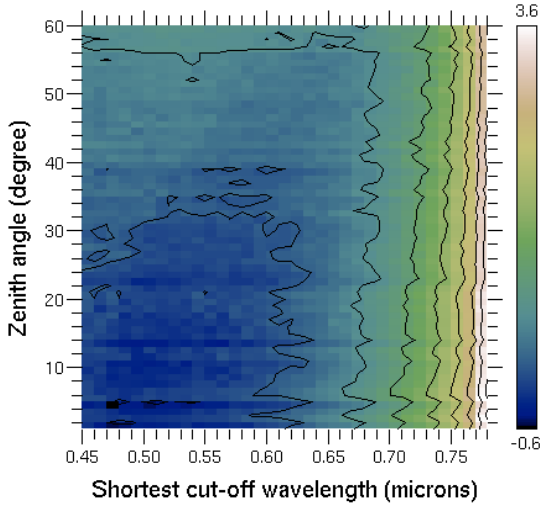

Figure 6: Magnitude loss when no ADC is used in photon noise regime, for a reference source effective temperature of 3300 K, with respect to the case with an ADC and a WFS bandpass of [0.45 μm – 0.8 μm], as a function of the shortest WFS cut-off wavelength and of the zenith angle. Contours are for a magnitude loss from -0.5 to 3.5 equally spaced by 0.5

Hence, for typical M stars of the main sequence, the lack of ADC induces a magnitude loss of ~0.1 mag (in the photon noise regime) for the design conditions at a zenith angle of 30°.

In the detector noise regime, the WFS noise σ^2 is proportional to $\theta_b^4/np^2(\lambda_{inf},\lambda_{sup})$. The loss in magnitude due to the atmospheric dispersion is then given by:

$$-2.5\log\left(\frac{np_{w/oADC}(\lambda_{min})}{np_{w/ADC}(0.45)}\sqrt{\frac{2\times f^4(z,0.45)}{f^4(z,0.45)+\Delta G^4(z,0.45)}}\right)$$

The following figure shows the magnitude loss when not using any ADC as a function of the shortest cut-off wavelength of the WFS bandpass.

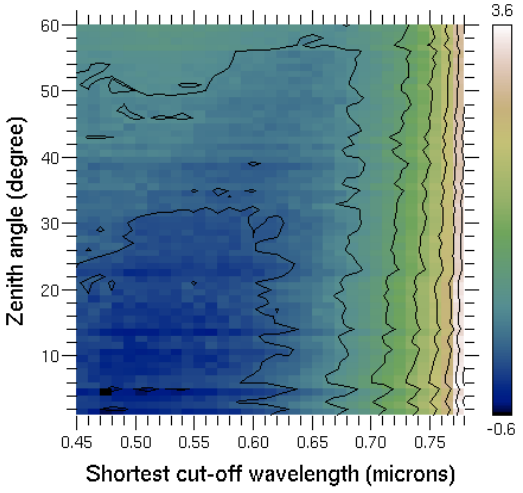

Figure 7: Magnitude loss when no ADC is used in detector noise regime, for a reference source effective temperature of 3300 K, with respect to the case with an ADC and a WFS bandpass of [0.45 μm – 0.8 μm], as a function of the shortest WFS cut-off wavelength and of the zenith angle. Contours are for a magnitude loss from -0.5 to 3.5 equally spaced by 0.5

Hence, for typical M stars of the main sequence, the lack of ADC induces a magnitude loss of ~0.1 mag (in the detector noise regime) for the design conditions at a zenith angle of 30°.

6 OPTICAL DESIGN

6.1 General aspects

The ELT optical behavior has been simulated using the data in AD8 and the Zemax file EELT_v.2.BDE.zmx.

Main characteristics:

- Nasmyth B
- Angular field of view: 10.0 arc minutes diameter (unvignetted)
- The entrance pupil size and location, 42-m diameter, on M1
- Focal ratio: 17.71
- Field curvature: 43.8 m (concave towards exit pupil)
- Plate scale: 1 arc second = 3.605 mm
- Exit pupil position: - 43.263 m
- Central obstruction: 9.2% introduced by M4 (pupil, central hole)

In our design (especially for the WFS), we consider the pupil is located on M4 adaptative mirror. Thus, M4 is conjugated to the lenslet array.

For all the optical data of the sub-systems listed hereafter:

- Distances, decenters, radii of curvature, diameters are in millimeters (mm).
- Rotations are in degrees (°).
- Rotations are done before decenters on a surface.
- Zero point is E-ELT Nasmyth focus.

6.2 The relay optics

6.2.1 Optical design detailed description

The optical relay is based on the concept of the Offner relay (mirrors M7, M8 and M9).

The optical layout is shown in the next two figures.

M7 and M9 are parts of the same concave spherical mirror.

M8 is a convex spherical mirror.

M10 is the folding mirror that creates a gravity invariant configuration for MICADO.

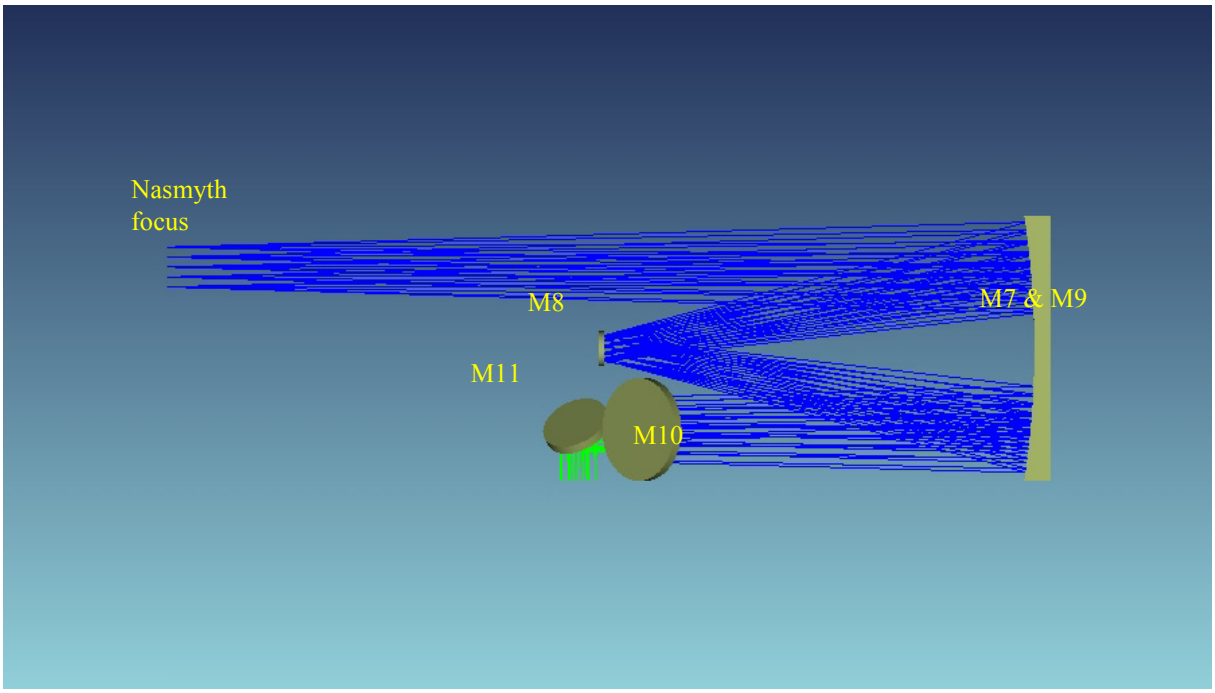

Figure 8: Relay optics layout, top view. Blue beams for MICADO channel, and Green beams for WFS channel

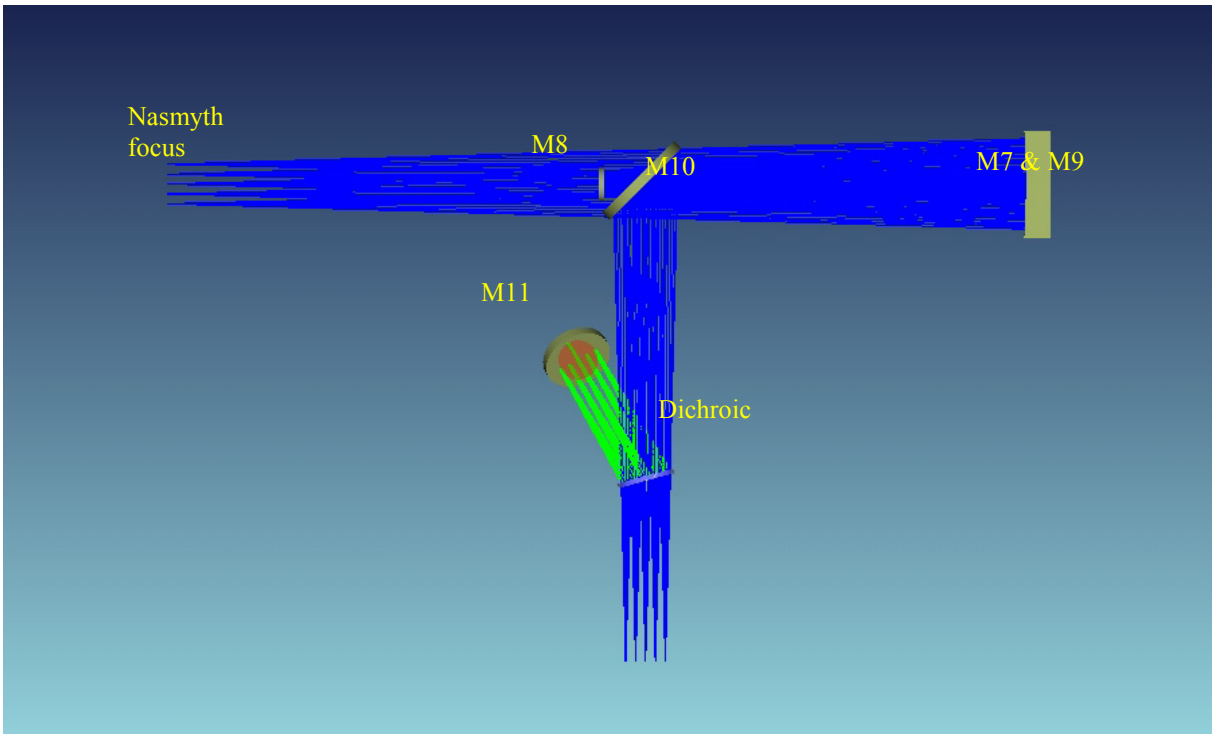

Figure 9: Relay optics layout, side view. Blue beams for MICADO channel, and Green beams for WFS channel.

The dichroic plate realizes the WFS pick-off: the spectral band [0.45 – 0.8 µm] is reflected, whereas the spectral band [0.8 – 2.32 µm] is transmitted towards MICADO. The dichroic is corrected for astigmatism and lateral chromatism.

Mirror M11 folds the beam in order that the WFS is horizontal.

The positions of the mirrors have been given in global vertex coordinates assuming a coordinate reference linked to the ELT focal plane.

Surface	X [mm]	Y [mm]	Z [mm]
0: Nasmyth focus	0	0	0
1: M7	0	330.8	-3559.4
2: M8	0	330.8	-1789.7
3: M9 (= M7)	0	330.8	-3559.4
4: M10	0	661.6	-1959.4
5: Dichroic S1	1200.0	661.6	-1959.4
6: Dichroic S2	1219.3	661.6	-1964.5
7: Focal plane MICADO	1965.1	661.6	-1959.8
8: M11	723.7	-	-
9: Focal plane WFS	723.7	-	-

Table 3: Coordinates of surfaces vertices.

The followings tables give the prescription data for the two relay channels.

Surface	Radius of curvature	Distance / next surf	Material	Diameter	Rotation	Decenter
0: Nasmyth focus	43800	-3559.4	Air	162.2		
1: M7	3359.4	1769.6	Refl	1080.0 x 440.0		330.8 (y)
2: M8	-1789.7	-1769.6	Refl	140.0		
3: M9 (= M7)	3359.4	1600.0	Refl	1080.0 x 440.0		330.8 (y)
4: M10	Plane	-1200.0	Refl	420.0	-45 (y)	
5: Dichroic S1	Plane	-20.0	Infrasil	240.0	15 (y)	
6: Dichroic S2	449621 (curv.x)	-	Air	240.0	0.20 (y)	
7:		-745.7	Air		-15.29 (y)	3.49 (x)
8: Image	Plane	-	Air	162.2		

Table 4: Optical prescription, relay optics, MICADO Channel.

Surface	Radius of curvature	Distance / next surf	Material	Diameter	Rotation	Decenter
0: Nasmyth focus	43800	-3559.4	Air	162.2		
1: M7	3359.4	1769.6	Refl	1080 x 440		330.8 (y)
2: M8	-1789.7	-1769.6	Refl	140		
3: M9 (= M7)	3359.4	1600.0	Refl	1080 x 440		330.8 (y)
4: M10	Plane	-1200.0	Refl	420	-45 (y)	
5: Dichroic S1	Plane	550.0	Refl	240	15 (y)	
6: M11	Plane	126.3	Refl	280	45 (x)	
7: Image	Plane	-	Air	162.2		

Table 5: Optical prescription, relay optics, WFS Channel.

Assuming a reflectivity of ~99% for the mirrors (protected silver/aluminium coated), a dichroic plate reflection of 98% in the visible, and a dichroic plate transmission of 95% in the infrared, the transmission of the relay mirrors + dichroic plate (+ M11 for the WFS channel) is equal to:

- 91% for the MICADO channel.
- 93% for the WFS channel.

6.2.2 Performance analysis

The spot diagrams for a field of view of ±22.5” × ±22.5” (rows) and wavelengths at 0.8, 0.95, 1.65 and 2.32 µm (columns) are shown in the next figure for MICADO channel.

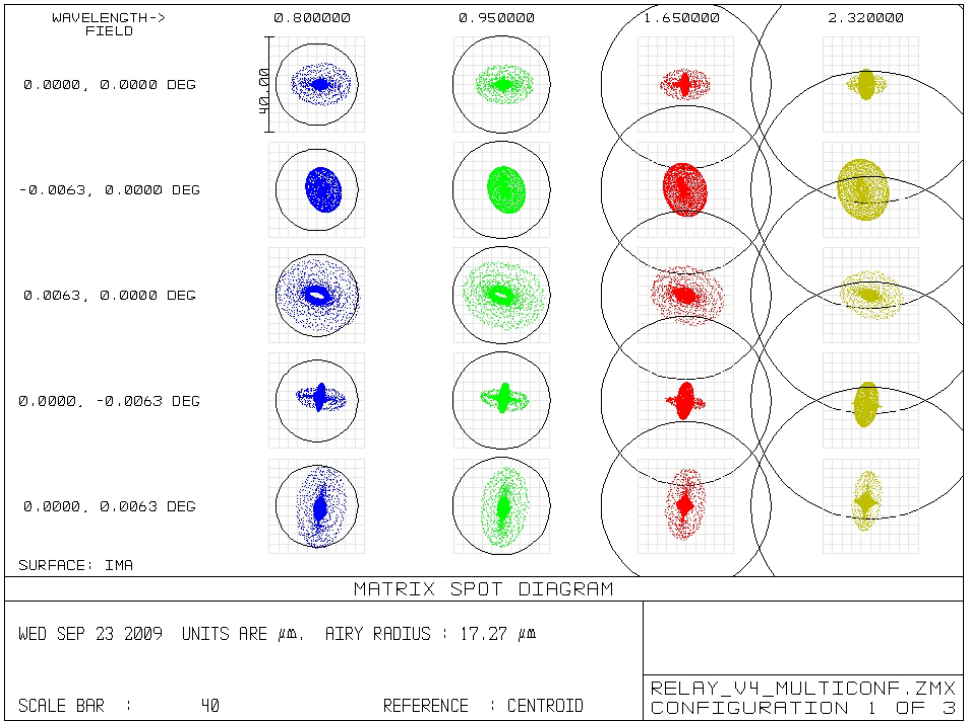

Figure 10: Spot diagrams for different wavelengths (columns) and different FOV (rows). Circles represent the AIRY disk at the correspondent wavelength. MICADO channel.

The Strehl ratio over the entire field of view at the shortest wavelength (0.8 µm) is shown in the next figure.

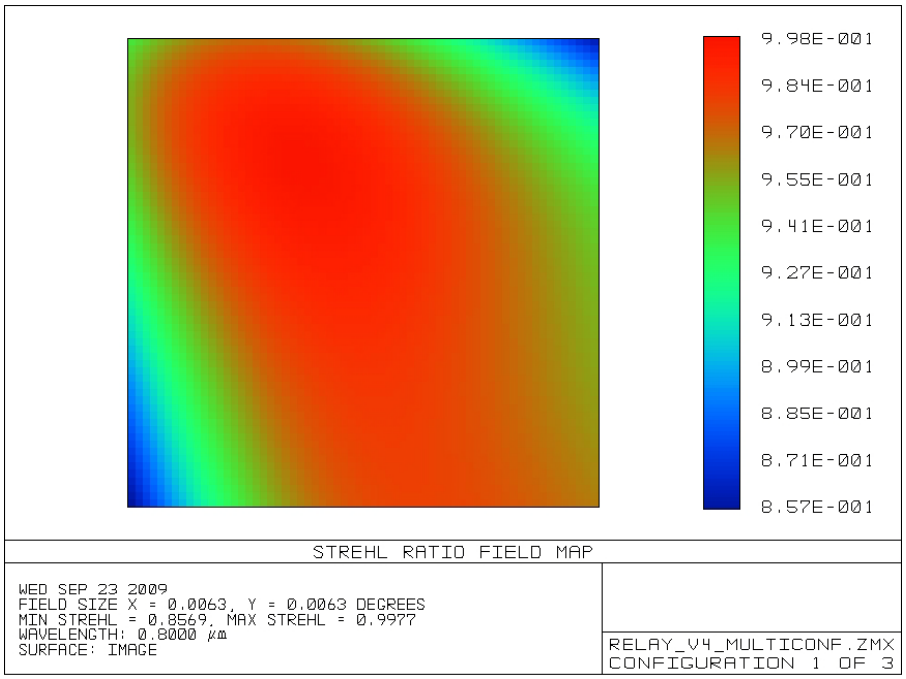

Figure 11: Strehl Ratio field map at wavelength 0.8µm, MICADO channel.

The worst value on the circular field of view is 95%, i.e. relay is diffraction limited over the entire field of view. Distorsion is very small (-0.004%) at the edge of the FoV. The spot diagram for the WFS channel is shown in the next figure.

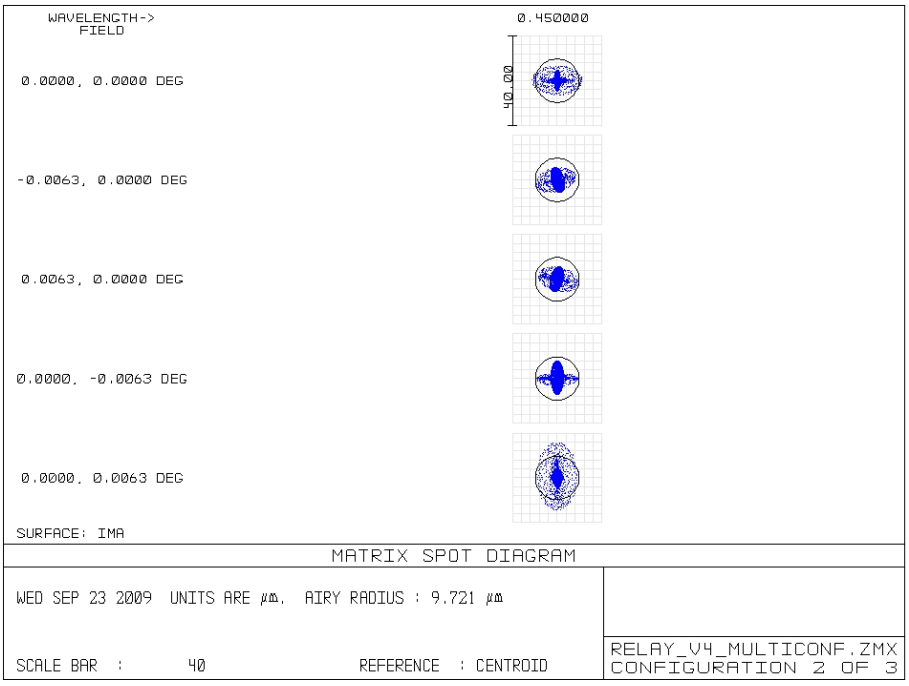

Figure 12: Spot diagrams at 0.45µm for different FOV (rows). Circles represent the AIRY disk at 0.45µm. WFS channel.

6.2.3 Tolerance analysis

A preliminary tolerance analysis has been performed using as a merit function the PSF Strehl ratio > 80%. A list of parameters has been defined corresponding to the errors in positioning (tilts and decenters) and manufacturing for all optical surfaces. All the surfaces are assumed to be independent, except M7 and M9 that are linked. The location of the focal plane has been assumed to be adjustable to the best focus position, allowing one to relax the tolerances.

When a rotation variation of a single surface is done, the rotation axis is located at the vertex of the surface. When a rotation variation of an optical element or of a group of elements is done, the rotation axis is located at the vertex of the first surface of the element.

The optical quality of each surface is set to λ/10 PTV (at 632.8nm).

The sensitivity analysis provides for each parameter the change in RMS wavefront errors and underlines the most sensitive parameters. The criteria of the PSF Strehl ratio > 80% has been checked *a posteriori* on the worst case of a Monte Carlo simulation of 100 trials. Details on the results are given in the following table.

Surface or element	Parameter		Value	Min	Max
M7 & M9	radius of curvature	mm	3359.4	-0.5	+0.5
	decenter z	mm	3359.4	-0.2	+0.2
	decenter x	mm	0	-0.2	+0.2
	decenter y	mm	330.8	-0.2	+0.2
	tilt x	degree	0	-0.2	+0.2
	tilt y	degree	0	-0.2	+0.2
M8	radius of curvature	mm	1789.7	-0.5	+0.5
	decenter z	mm	1769.6	-0.2	+0.2
	decenter x	mm	0	-0.2	+0.2
	decenter y	mm	0	-0.2	+0.2
	tilt x	degree	0	-0.2	+0.2
	tilt y	degree	0	-0.2	+0.2
M10	decenter z	mm	1600.0	-0.2	+0.2
	decenter x	mm	0	-0.2	+0.2
	decenter y	mm	0	-0.2	+0.2
	tilt x	degree	0	-0.1	+0.05
	tilt y	degree	-45.0	-0.1	+0.01
Dichroic	radius of curvature (rear face)	mm	444621	-50	+50
	decenter z	mm	1200.0	-0.2	+0.2

	decenter x	mm	0	-0.2	+0.2
	decenter y	mm	0	-0.2	+0.2
	tilt x	degree	0	-0.2	+0.2
	tilt y	degree	-15.0	-0.2	+0.2
	tilt of rear face	degree	0.2	-0.03	+0.03
	index (nd)		1.459	-0.001	+0.001
M11	decenter z	mm	550.0	-0.2	+0.2
	decenter x	mm	0	-0.2	+0.2
	decenter y	mm	0	-0.2	+0.2
	tilt x	degree	45.0	-0.2	+0.2
	tilt y	degree	0	-0.2	+0.2

Table 6: Optical tolerances for the relay optics.

The back focal distance is adjusted within the range [-2.0; +2.0] mm. The spot diagrams and Strehl ratio map obtained with the worst case are shown in the two following figures.

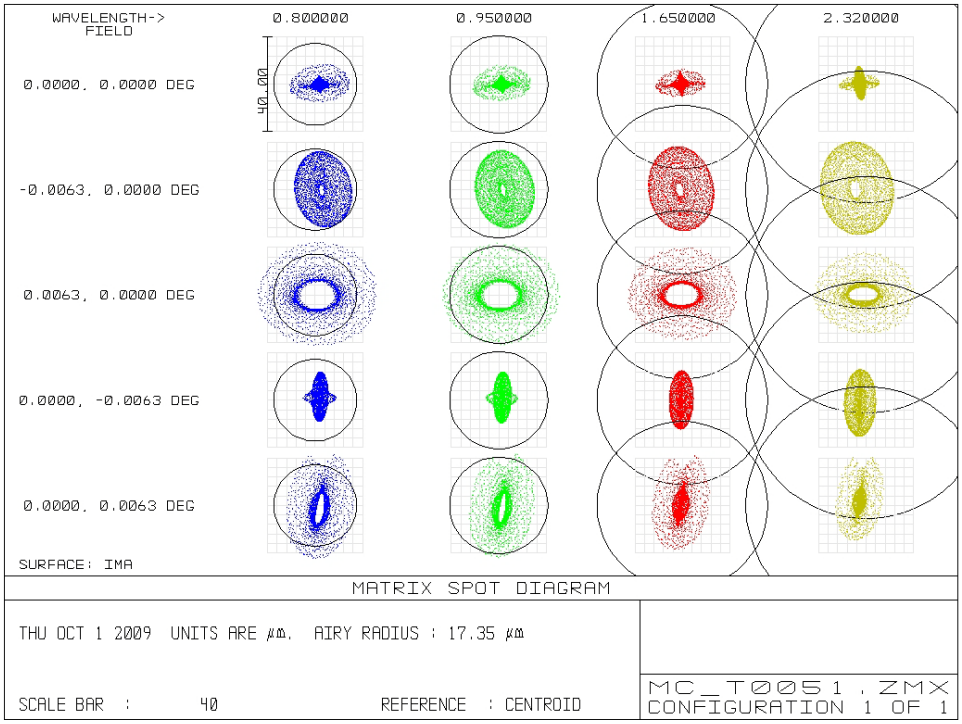

Figure 13: Spot diagrams for different wavelengths (columns) and different FOV (rows), worst trial of Monte-Carlo simulation. Circles represent the AIRY disk at the corresponding wavelength MICADO channel.

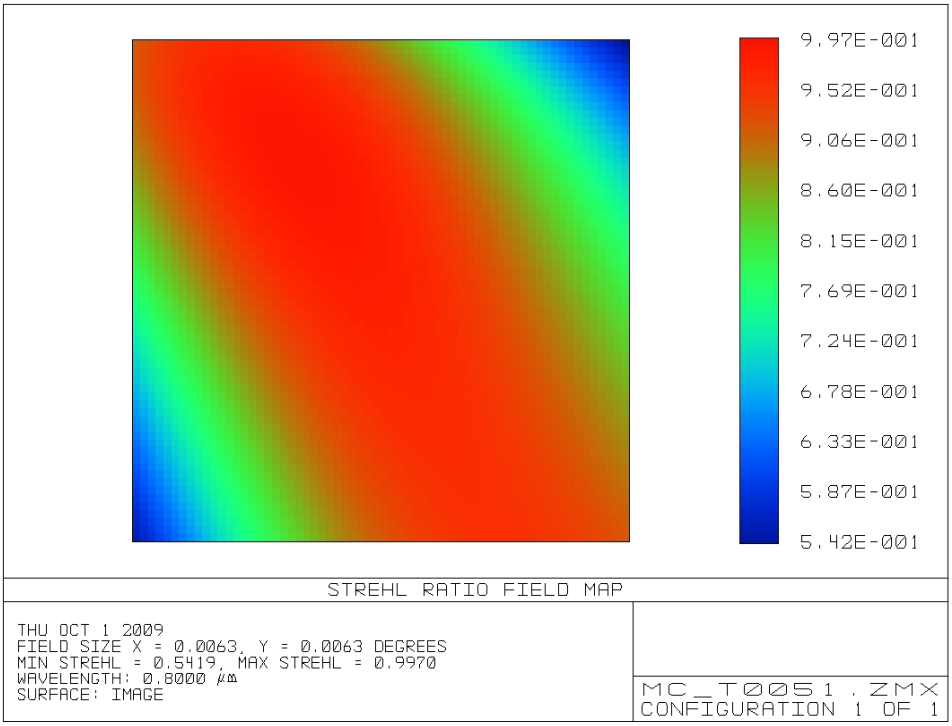

Figure 14: Strehl Ratio field map at wavelength 0.8µm, worst trial of Monte-Carlo simulation MICADO channel.

The Strehl ratio remains higher than 80% at 0.8µm on the 45 arcsec circular FoV.

6.2.4 Estimation of cost

The cost of the relay optics is estimated to 100k€. The details are given in the following table:

Element	Type	Dimensions [mm]	Thickness [mm]	Material	Cost [k€]
M7 & M9	Spherical concave mirror	1080 x 440	80	zerodur	30
M8	Spherical convex mirror	ϕ 140	20	zerodur	10
M10	Plane mirror	ϕ 420	60	zerodur	15
M11	Plane Mirror	ϕ 280	45	zerodur	5
Dichroic	Prismatic plate with a cylindrical rear face	ϕ 240	20	infrasil	40
TOTAL					100

Figure 15: Cost estimate of the relay optics parts

6.3 The WFS optics

6.3.1 Optical design detailed description

The visible WFS is Shack-Hartmann type and it is fed by the dichroic in reflection (F/17.7).

The optical train consists of an optical derotator to compensate for the pupil rotation, a pupil imaging lens, a lenslet array and the detector. The WFS layout is shown in the following figure.

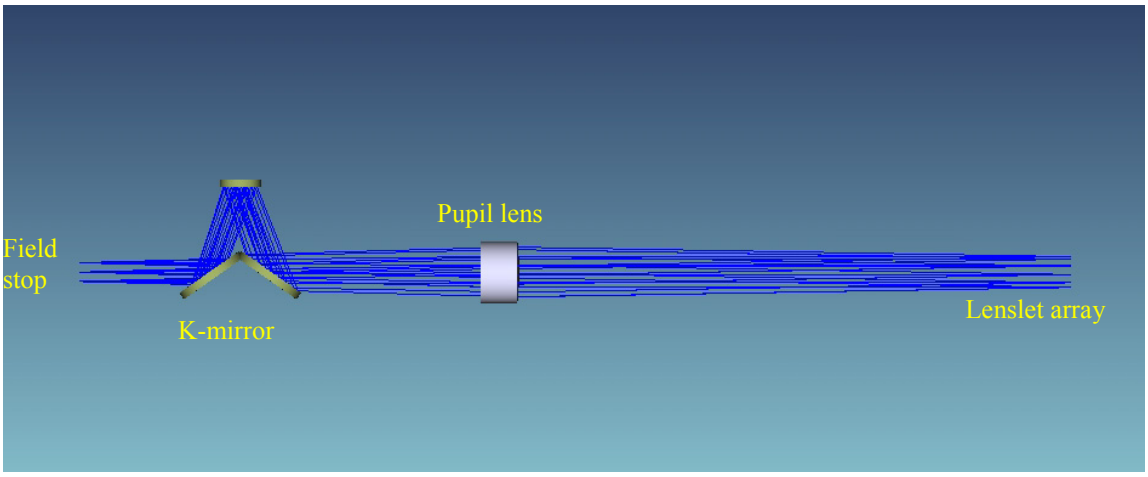

Figure 16: WFS optics layout, side view.

The FoV is 1.8 arcsec and the optical design has been optimized for the wavelength range between 0.45 and 0.8 μm. The optical derotator is a K-mirror located after the relay focus.

Immediately after is placed the pupil lens to re-image the E-ELT adaptative mirror (M4) on the lenslet array. At the end of the optical train is placed the lenslet array. Prescription data can be found in the following tables.

Surface	Radius of curvature	Distance / next surf	Material	Diameter	Rotation
0: field stop	Plane	-50	Air	3.3	
1: K-mirror M12	Plane	35	Refl	28.0	-55 (x)
2: K-mirror M13	Plane	-35	Refl	16.0	20 (x)
3: K-mirror M14	Plane	80.7	Refl	28.0	-55 (x)
4: Pupil lens S1	335.7	5	Schott FK51	24.0	
5: Pupil lens S2	-54.0	5	Schott KZFSN5	24.0	
6: Pupil lens S3	5740.8	5	Schott F2	24.0	
7: Pupil lens S4	-97.6	212.8	Air	24.0	
8: Pupil image	Plane	-	Air	12.096	

Table 7: Optical prescription, WFS K-mirror and pupil lens.

Parameter	Value
Number of lenses	84 x 84
Single lens diameter	0.144 mm
Singlelens focal length	5.00 mm
Single lens focal ratio	F/33
Lenslent diameter	12.096
Lenslet Thickness	1.00 mm
Lenslet back focal distance	4.00 mm
Material	Fused Silica

Table 8: Optical prescription, WFS lenslet array.

Assuming a reflectivity of 97% for the mirrors, and an AR coating with a transmission of 98.5% for the visible optics, the transmission of the WFS optics is equal to 86%.

6.3.2 Performance analysis

In the next figure, the footprints of the beam at the pupil image location for different off-axis fields are superimposed. The maximum circular aperture diameter is 12.12 mm.

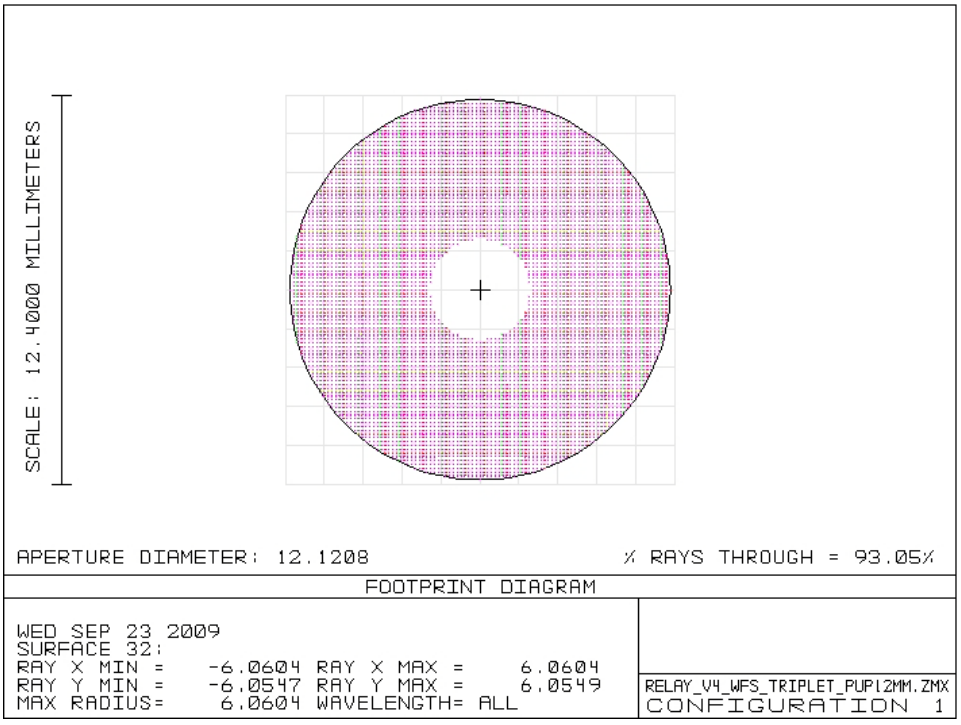

Figure 17: Pupil image footprint on lenslet array, WFS.

The following figure shows the spot diagrams obtained when the object is placed on M4 and pupil at Nasmyth focus:

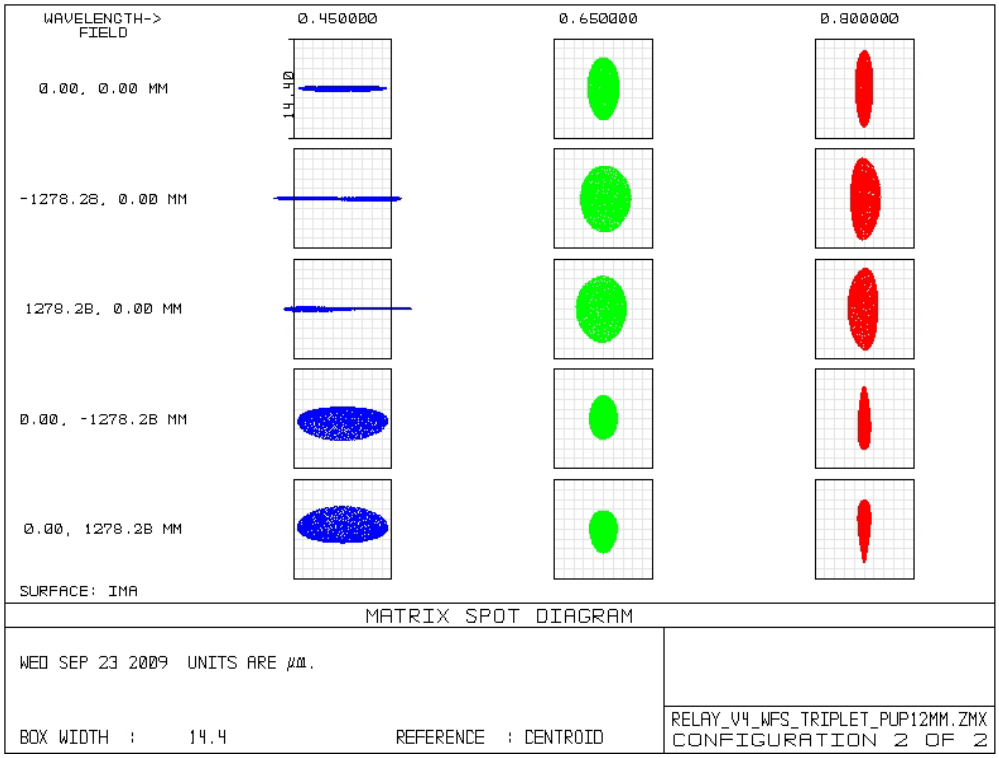

Figure 18: Spot diagrams for different wavelengths (columns) and different FOV (rows). Boxes represent 1/10 of a subaperture, i.e. 14.4µm

6.3.3 Tolerance analysis

The same analysis has been conducted than for the relay optics. The distance between the K-mirror and the lens pupil and between the lens pupil and pupil image are set as compensators. They are optimised within the range [-0.2;+0.2mm]. The results are summarized in the following table:

Surface or element	Parameter		Value	Min	Max
M12	decenter z	mm	0	-0.05	+0.05
	decenter x	mm	0	-0.2	0.2
	decenter y	mm	0	-0.2	0.2
	tilt x	degree	55	-0.01	+0.01
	tilt y	degree	0	-0.01	+0.01
M13	decenter z	mm	35	-0.05	+0.05
	decenter x	mm	0	-0.2	0.2
	decenter y	mm	0	-0.2	0.2
	tilt x	degree	20	-0.01	+0.01
	tilt y	degree	0	-0.01	+0.01

M14	decenter z	mm	35	-0.05	+0.05
	decenter x	mm	0	-0.2	0.2
	decenter y	mm	0	-0.2	0.2
	tilt x	degree	55	-0.01	+0.01
	tilt y	degree	0	-0.01	+0.01
K Mirror	decenter z	mm	50	-0.5	+0.5
	decenter x	mm	0	-0.05	+0.05
	decenter y	mm	0	-0.05	0+.05
	tilt x	degree	0	-0.01	+0.01
	tilt y	degree	0	-0.01	+0.01
Pupil lens S1	radius of curvature	mm	335.7	-0.3	+0.3
	tilt x	degree	0	-0.05	+0.05
	tilt y	degree	0	-0.05	+0.05
	Index (nd)			-0.0005	+0.0005
Pupil lens S2	radius of curvature	mm	-54.01	-0.05	+0.05
	decenter z	mm	5.0	-0.2	+0.2
	tilt x	degree	0	-0.05	+0.05
	tilt y	degree	0	-0.05	+0.05
	Index			-0.0005	+0.0005
Pupil lens S3	radius of curvature	mm	5740.8	-0.5	+0.5
	decenter z	mm	5.0	-0.2	+0.2
	tilt x	degree	0	-0.05	+0.05
	tilt y	degree	0	-0.05	+0.05
	Index			-0.0005	+0.0005
Pupil lens S4	radius of curvature	mm	-97.59	-0.05	+0.05
	decenter z	mm	5.0	-0.2	+0.2
	tilt x	degree	0	-0.05	+0.05
	tilt y	degree	0	-0.05	+0.05
Pupil lens	decenter z	mm	80.7	-0.2	+0.2
	decenter x	mm	0	-0.05	+0.05
	decenter y	mm	0	-0.05	+0.05
	tilt x	degree	0	-0.05	+0.05
	tilt y	degree	0	-0.05	+0.05

Table 9: Optical tolerances for the relay optics.

The main degradation of the optical performances is to the pupil image quality, and more precisely the chromatism. On the worst case of the Monte-Carlo simulation (100 trials), the chromatism is of the order of 1/10th of a subaperture, as shown in the following figure.

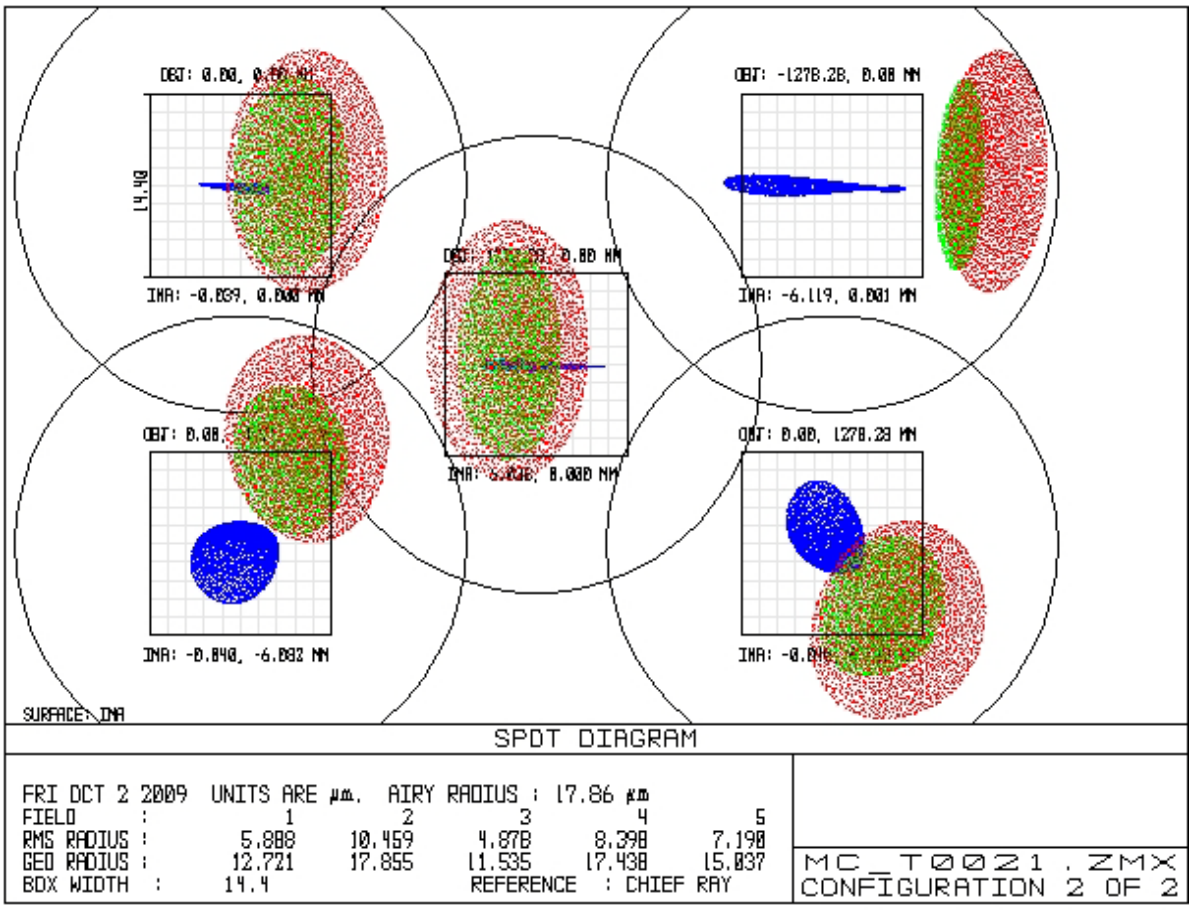

Figure 19: Spot diagrams for different wavelengths (columns) and different FOV (rows). Boxes represent 1/10 of a subaperture, i.e. 14.4µm. Worst case of the Monte-Carlo simulation (100 trials).

6.3.4 Estimation of cost

The cost of the WFS optics (K-mirror, pupil lens and lenslet array) is estimated to 70k€. The details are given in the following table:

Element	Type	Dimensions [mm]	Thickness [mm]	Material	Cost [k€]
K mirror	3 plane mirrors	ϕ 28, 16, 28	3 for each	zerodur	60
Pupil lens	Triplet	ϕ 24	5 for each lens	FK51, KZFSN5, F2	10
TOTAL					70

Table 10: Cost estimate of the WFS (not including the detector)

7 MECHANICAL DESIGN

7.1 Description

7.1.1 The support structure

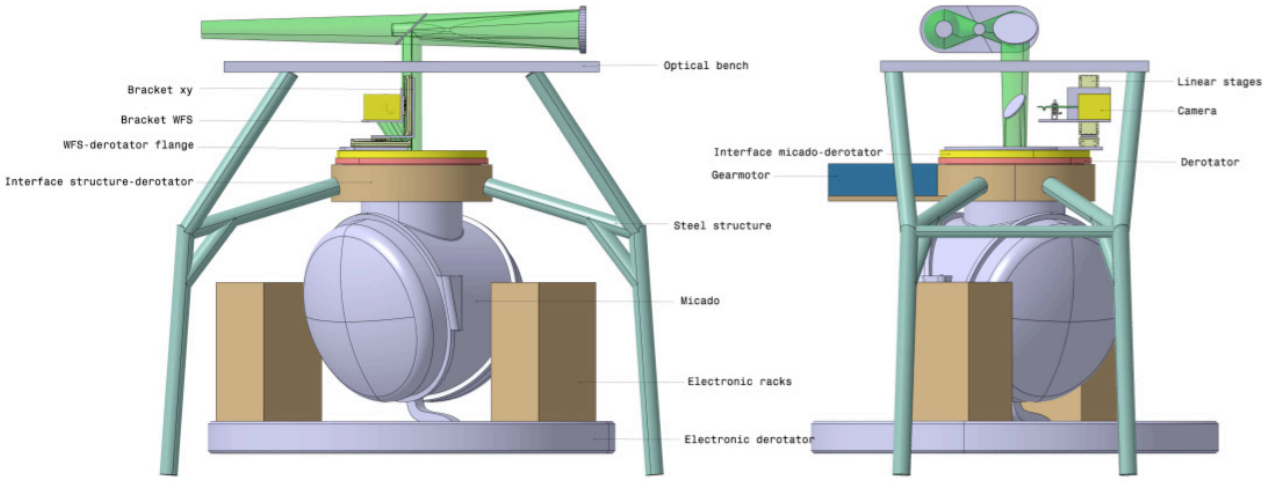

Figure 20: Global view of MICADO and SCAO module support structure (without the MICADO calibration unit on the relay optics bench)

MICADO + SCAO module support structure is a steel two-stage arch-like structure. The upper stage supports the relay optics bench and the lower one support the derotator + the WFS + MICADO.

This arch-like structure has been preferred to an hexapod structure to facilitate the mounting of MICADO and because of the use of a crane to mount MICADO. This hyperstatic mount hence gives more stability to the assembly.

The MICADO cryostat is fixed together to the interface MICADO-derotator part, which is fixed together with the derotator. Thus the free rotation of the cryostat is possible.

The following table gives the estimated mass and cost of the support structure.

Item	Mass (kg)	Cost (euros)
Steel structure	1300	15000
Interface structure-derotator	700	6000
Total mounting structure	**2000**	**21000**

Table 11: Mass and cost estimates of the support structure

7.1.2 The relay optics

The relay optics optical bench has been chosen among product but it could be a customized design with an honeycomb structure to decrease the mass. The size of the bench (2.5m x 3.5m) has been chosen to allow a well-balanced equilibrium given the optics lying on it. A hole in the

center of the bench has been added for the optical beam going down to MICADO and the WFS.

The following table gives the estimated mass and cost of the relay optics.

Item	Mass (kg)	Cost (euros)
Optical bench (2.5m x 3.5m)	1300	8000
M7-M9	100	30000
M7-M9 mount	30	10000
M10	15	15000
M10 mount	15	5000
M8	1	10000
M8 mount	10	3000
Total	**1471**	**81000**

Table 12: Mass and cost estimates of the relay optics assembly

7.1.3 The derotator

The derotator is a kind of ball bearing made of two components:

- an internal ring fixed to the interface structure-derotator part,
- an external ring supporting the interface MICADO-derotator part.

This external ring is in fact a wheel allowing the transmission with the gearmotor.

The following table gives the estimated mass and cost of the derotator.

Item	Mass (kg)	Cost (euros)
Derotator	185	4300
Interface MICADO - derotator	325	10000
Gearmotor	100	7000
Total Derotator – MICADO flange package	**610**	**42300**

Table 13: Mass and cost estimates of the derotator

7.1.4 The WFS

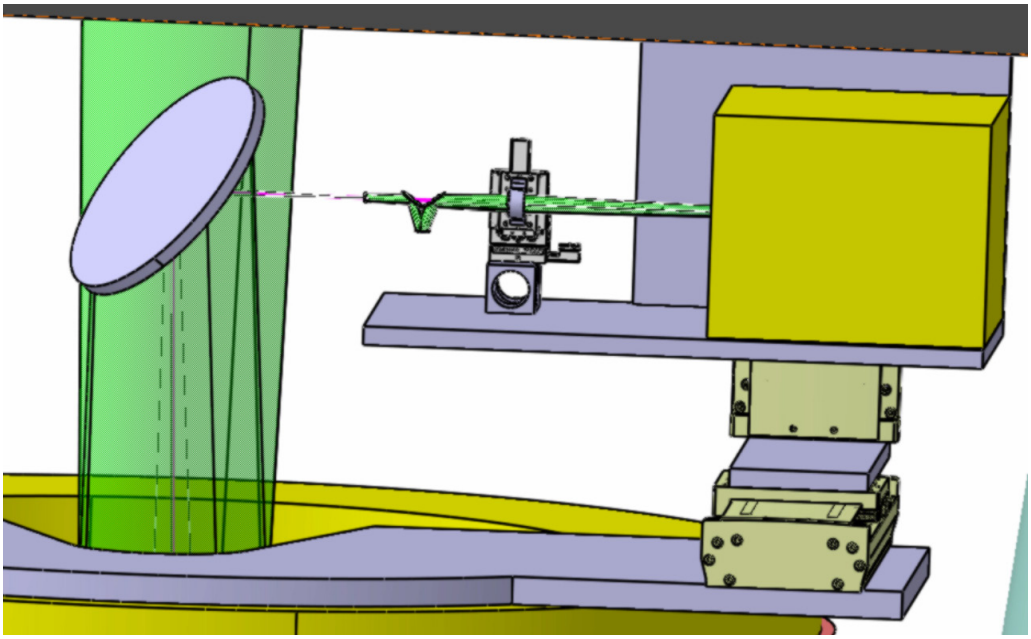

Figure 21: View of the WFS. On the left, the M11 mirror. On the right, the yellow box is the camera. At the centre, the field stop, the K-mirror and the triplet. The two beige parts are the linear stages allowing the WFS to move in the field (for reference star pick up and offsets/dithers)

The dichroic plate, the WFS and the M11 mirror are fixed together with the interface MICADO-derotator and then rotate together with MICADO.

The WFS includes the triplet, the cold stop and the K-mirror, which are fixed together. The WFS has an XY motion allowed by two linear stages in front of the M11 mirror. Commercial linear stages (Newport, M-IMS 300ML) fulfill the specifications given in Section 5.4.1 and have then been adopted.

The following table presents the estimated cost and cost of the WFS.

Item	Mass (kg)	Cost (euros)
Camera	10	140000
Linear stages (X & Y)	34	14200
Bracket xy	6.5	700
Bracket WFS	20	1000
WFS – derotator flange	60	2000
Dichroic plate + mount	10	45000
M11 mirror + mount	15	12000

Triplet + mount	5	11000
K-mirror + mount	6	62000
Cold stop + mount	2	1000
Total	**168,5**	**298900**

Table 14: Mass and cost estimate of the WFS. The camera cost includes the detector and the electronics and has been provided by E. Marchetti

7.2 Mechanical analysis

We describe in this section a mechanical analysis of the support structure to evaluate deformations and constraints according to the applied boundary conditions. This is a first estimation and only small perturbations in a static domain are considered.

7.2.1 The geometrical dimensions and the material properties

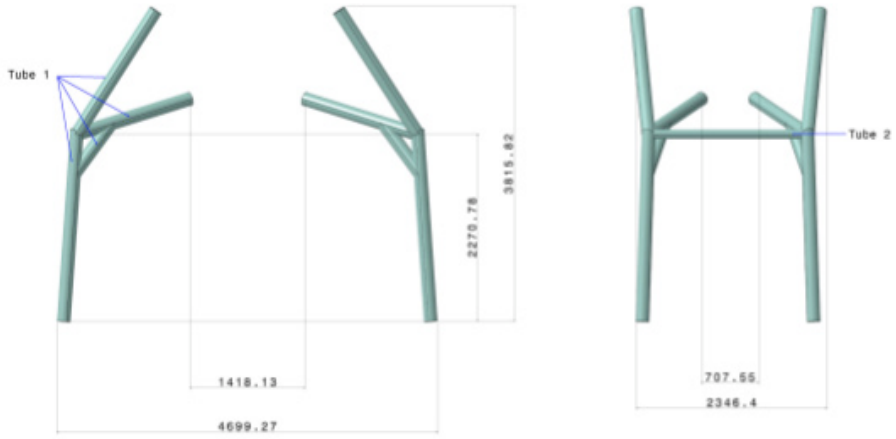

Figure 22: Dimensions of the two-stage arch-like structure

The structure is made of two different kinds of steel pipe:

- Tube 1 has a 160 mm outside diameter with a 145 mm internal diameter
- Tube 2 has a 114 mm outside diameter with a 96 mm internal diameter.

The mechanical properties for the steel are:

Young's modulus (Mpa)	200000
Poisson's ratio	0.3
Elastic limit (MPa)	300
Density	7.85

Table 15: Mechanical properties of an usual steel

7.2.2 The mesh and applied loads

The mesh includes only beam elements and two rigid bodies: the cryostat+WFS+derotator+interface-structure-derotator part, for a total load of 50000 N, and the optical bench+optics+MICADO calibration unit part for a total load of 16000 N (15000 N for the optical bench+optics, 1000 for the MICADO calibration unit). The four supports are blocked.

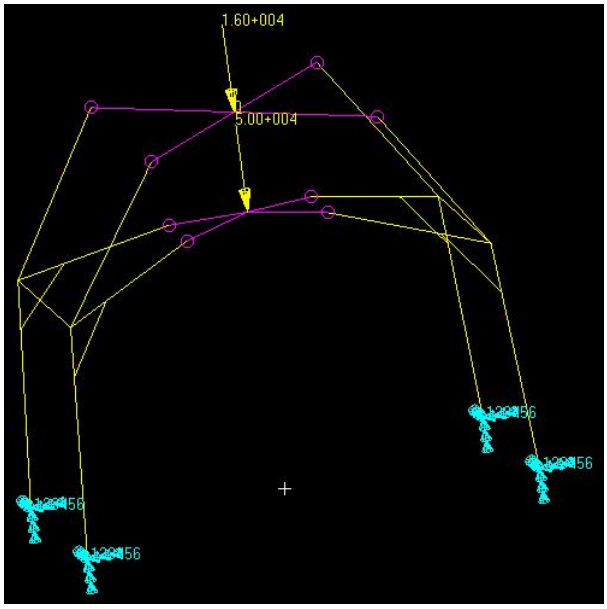

Figure 21: Mesh and boundary conditions of the structure model

7.2.3 Deformation

The max deflection is around 1.81 mm corresponding to the part where the cryostat hangs.

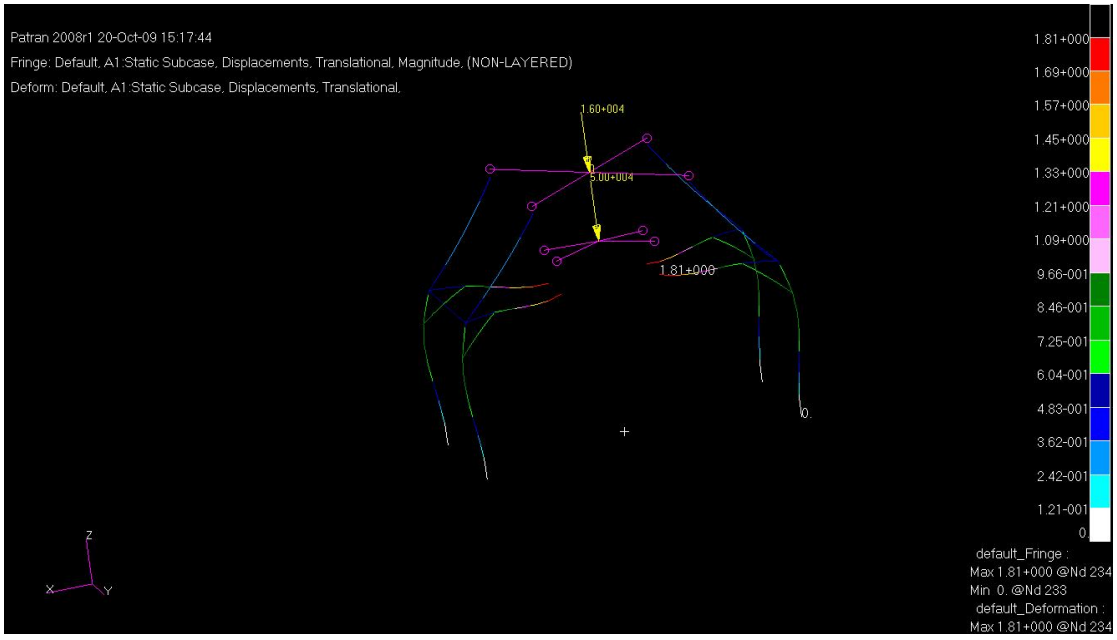

Figure 22: Deformation (in mm) of the structure model

7.2.4 Constraints

The max Von Mises constraints are around 69 MPa. The max Von Mises constraints of the structure are 4 times weaker than the elastic limit of usual steel.

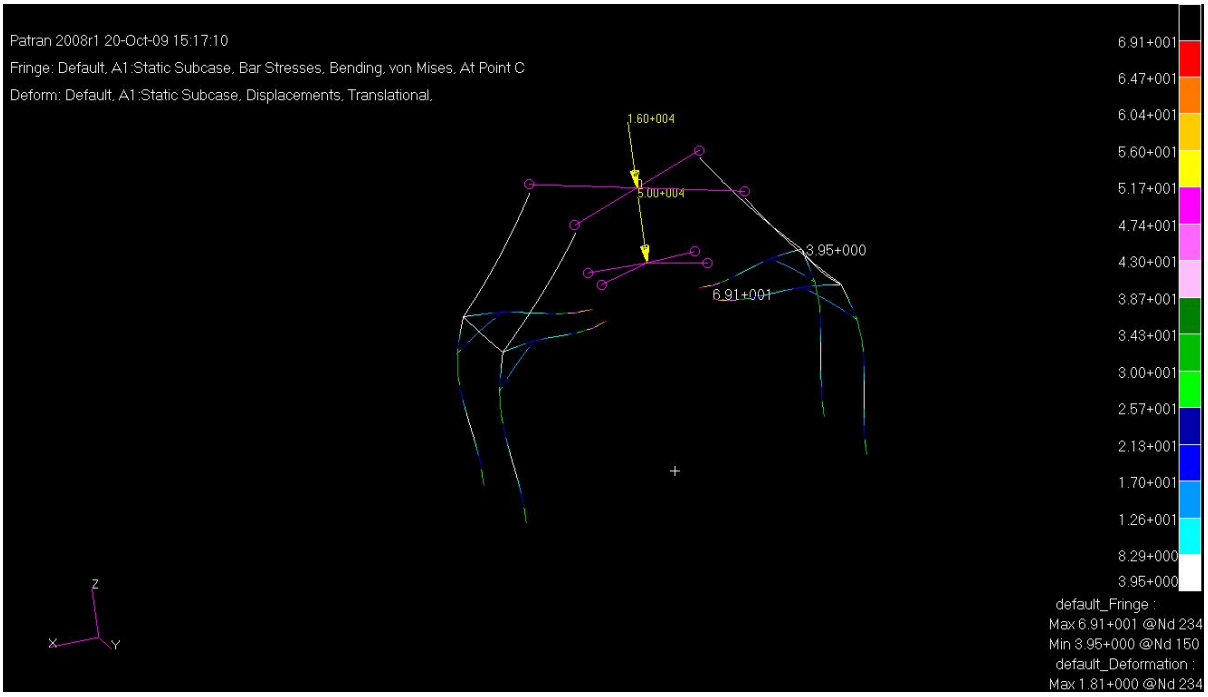

Figure 23: Von Mises Constraints of the structure model (MPa)

8 THERMAL ANALYSIS IN THE K-BAND

In this Section, we study the K-band thermal emission of the SCAO module seen by MICADO. This analysis is done with the following assumptions:

- atmospheric transmission: T_{atm}=95%,
- K-band zeropoint from AD10: F_0=4.37×10^9 photons/s/m^2/µm
- K-band sky brightness (AD6): m_{sky}=13 arcsec^{-2}
- MICADO transmission T_{mic}: 5 warm glass optics (one ADC and the entrance window) with individual transmissions of 98%, 5 cold aluminium-coated mirrors (transmission profile from AD10), a cold K-band filter (transmission profile from AD10) and a detector (quantum efficiency of 92%),
- telescope transmission T_{tel}: five mirrors with protected silver/aluminium coatings (transmission profile from AD10),
- telescope area A_{tel}=1276.82 m^2 (AD10),
- SCAO relay optics transmission T_{relay}: 4 relay optics mirrors with protected silver/aluminium coatings (transmission profile from AD10),
- SCAO dichroic plate transmission towards MICADO: T_{dichro}=95%, SCAO dichroic plate reflection: R_{dichro}=5%, diffusion on the SCAO dichroic plate: ε_{dif}=0.5%

- Glass transmission: T_g=98%, intrinsic glass transmission: T_{ig}=99.5%
- Pixel scale (primary arm): *pscl*=3 mas/pixel,
- Pixel size: 15 microns, hence a pixel area $A_{pix}=2.25\times10^{-10}$ m^2
- Telescope focal ratio: 18.85
- MICADO linear scale: 3838 microns/arcsec

The f/ratio of warm beam on the detector is then 24.557 (18.85×15/3838/0.003), leading to a corresponding solid angle of 1.302×10^{-3} st ($\pi/4/24.557^2$) and then to a corresponding pixel area-solid angle product receiving warm radiation: $A_{pix}.\Omega_{pix}=2.930\times10^{-9}$ cm^2.st.

The sky emission is obtained by multiplying the sky emission outside the atmosphere (from its magnitude) by the atmosphere, telescope, SCAO and MICADO transmissions.

$$F_{sky} = \int_{\text{K-band}} T_{atm}.T_{tel}(\lambda).T_{relay}(\lambda).T_{dichro}.T_{mic}(\lambda).10^{-0.4\,m_{sky}}.F_0.A_{tel}.pscl^2.d\lambda$$

The telescope thermal emission is given by integrating over the K-band a Planck law $PL(\lambda,\theta)$ at the ambient temperature θ_{amb}, multiplied by the telescope emissivity ε_{tel} (=1-T_{tel}) and the SCAO and MICADO transmissions.

$$F_{tel} = \int_{\text{K-band}} T_{relay}(\lambda).T_{dichro}.T_{mic}(\lambda).PL(\lambda,\theta_{amb}).A_{pix}.\Omega_{pix}.\epsilon_{tel}.d\lambda$$

The SCAO thermal emission is given by integrating over the K-band a Planck law at the ambient temperature, multiplied by the SCAO emissivity ε_{scao} (=1-$T_{relay}.T_{dichro}$) and the MICADO transmission.

$$F_{scao} = \int_{\text{K-band}} T_{mic}(\lambda).PL(\lambda,\theta_{amb}).A_{pix}.\Omega_{pix}.\epsilon_{scao}.d\lambda$$

The MICADO warm optics thermal emission is given by integrating over the K-band a Planck law at the ambient temperature, multiplied by the MICADO warm optics emissivity ε_{wmic} (=1-T_{ig}^5) and the MICADO transmission.

$$F_{mic} = \int_{\text{K-band}} T_{mic}(\lambda).PL(\lambda,\theta_{amb}).A_{pix}.\Omega_{pix}.\epsilon_{wmic}.d\lambda$$

The two next figures represent the different K-band thermal emissions and the SCAO thermal emission compared to 50% and 10% of the sky+telescope thermal emission.

MAORY thermal emission top-level requirement states that the AO module thermal emission should not exceed 50% (with a goal of 10%) of the sky+telescope thermal emission. Adopting the same requirement, it then comes that the 50% requirement is then met for ambient temperatures up to about 17°C and the 10% requirement is met for ambient temperatures up to about -6°C.

Four different options could be considered to decrease the SCAO module background:

- option 1: like in NAOS, implement on the back side of the dichroic plate (the side in front of MICADO) a device - a "background limiter" - that fills up the field of view of MICADO, radiates a very small number of photons and is as black as possible to prevent light scattering. In that case, the SCAO module thermal emission is the sum of:
    - the relay optics mirror emission, at ambient temperature, transmitted by the dichroic plate towards MICACO, with ε_{relay}=1- T_{relay},

$$\int_{\text{K-band}} T_{mic}(\lambda).T_{dichro}.PL(\lambda,\theta_{amb}).A_{pix}.\Omega_{pix}.\epsilon_{relay}.d\lambda$$

    - the background limiter emission, at the background limiter temperature θ_{BGL}, reflected by the dichroic plate towards MICADO,

$$\int_{\text{K-band}} T_{mic}(\lambda).R_{dichro}.PL(\lambda,\theta_{BGL}).A_{pix}.\Omega_{pix}.d\lambda$$

    - the contribution at ambient temperature of diffusion (0.5% emission),

$$\int_{\text{K-band}} T_{mic}(\lambda).PL(\lambda,\theta_{amb}).\epsilon_{dif}.A_{pix}.\Omega_{pix}.d\lambda$$

- option 2: place all the relay optics mirrors and the dichroic plate inside a cooled enclosure. In that case, the SCAO thermal emission is the sum of:
    - the emission at ambient temperature of the enclosure entrance window transmitted by the SCAO module (4 mirrors plus dichroic plate) and the enclosure exit window, with ε_{ig}=1- T_{ig},

$$\int_{\text{K-band}} T_g.T_{relay}(\lambda).T_{dichro}.T_{mic}(\lambda).PL(\lambda,\theta_{amb}).\epsilon_{ig}.A_{pix}\Omega_{pix}.d\lambda$$

    - the emission at the cooled enclosure temperature θ_{scao} of the SCAO module transmitted by the enclosure exit window,

$$\int_{\text{K-band}} T_g.T_{mic}(\lambda).PL(\lambda,\theta_{scao}).\epsilon_{scao}.A_{pix}\Omega_{pix}.d\lambda$$

    - the contribution at ambient temperature of the enclosure exit window emission, assuming an exit window emission equal to ε_g=1- T_g and not ε_{ig} since light can be back-reflected by this window downwards MICADO,

$$\int_{\text{K-band}} T_{mic}(\lambda).PL(\lambda,\theta_{amb}).\epsilon_g.A_{pix}\Omega_{pix}.d\lambda$$

- option 3: place the dichroic plate inside the MICADO cryostat, assuming the MICADO ADC would be also cooled. In that case, the SCAO thermal emission is reduced to the relay optics mirror emission at ambient temperature. The cold optics (inside MICADO cryostat) transmission would then be modified by a factor corresponding to the dichroic plate infrared transmission and the ADC transmission.

$$\int_{\text{K-band}} T_{mic}(\lambda).PL(\lambda,\theta_{amb}).\epsilon_{relay}.A_{pix}\Omega_{pix}.d\lambda$$

- option 4: modify the SCAO module design to use a dichroic plate reflecting the infrared light towards MICADO (instead of transmitting it in the current design) and transmitting the visible light towards the WFS (instead of reflecting it in the current design). From the MAORY study (AD11), one could expect a dichroic plate infrared reflection of 98%. This dichroic plate being made in BK7, one could expect a visible transmission of 98%.

The next two figures show the SCAO module thermal emission for the first three options (plus the baseline). The 10% requirement is then reached for ambient temperatures up to 2°C using a background limiter at -30°C, up to 9°C placing SAMI inside a cooled enclosure at -30°C and up to 5°C placing the dichroic plate inside the MICADO cryostat.

In practical, the option 1 would require including this background limiter inside the derotator structure or at the level of the MICADO cryostat itself. A precise mechanical analysis, taking into account the low inclination of the dichroic plate, is required to check for the possibility of such an implementation. The option 2 would require using an enclosure cooled on a rather large surface: the relay optics bench is 2.5m × 3.5 m. Such a large enclosure has been contemplated by MAORY (AD11), with an additional mass of 3350 kg. Though an additional difficulty is to include the dichroic plate inside this enclosure, the dichroic plate being located inside the derotator structure. The option 3 would require modifying the MICADO cryostat design. The option 4 would require making a new SCAO design and analysis.

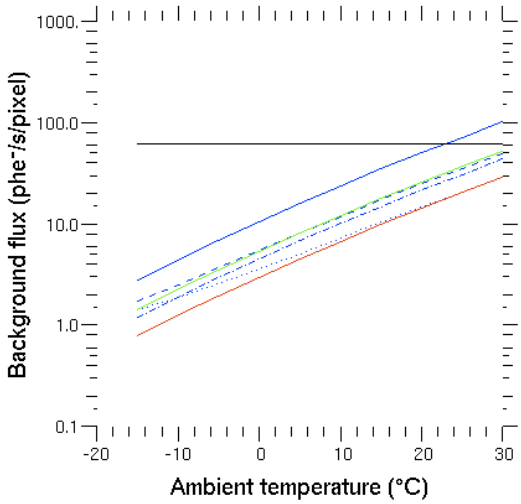

Figure 23: K-band thermal emissions in phe-/s/pixel for different ambient temperature in °C. In red the MICADO warm optics thermal emission, in black the (constant) sky thermal emission and in green the telescope thermal emission. In blue the SCAO thermal emissions: the continuous line is for the current design, the dash line for the option 1 (background limiter), the dotted line for the option 2 (cooled enclosure) and the dotted-dashed line for the option 3 (dichroic plate inside MICADO cryostat)

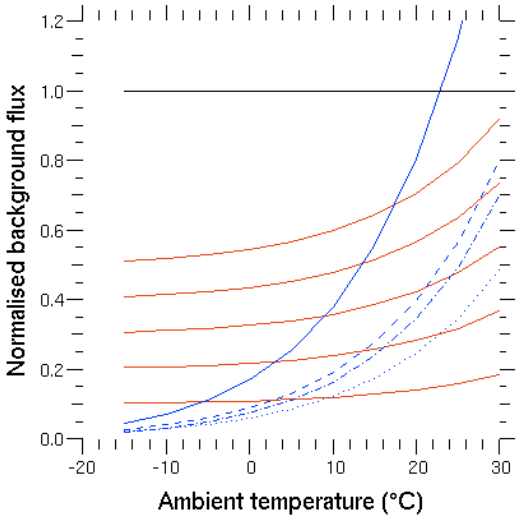

Figure 24: K-band thermal emissions, normalized to the sky one's. In black, the sky thermal emission In red, 50%, 40%, 30%, 20% and 10% of the sky+telescope thermal emission. In blue the SCAO thermal emissions for the current design and the options 1, 2 and 3, as in Fig. 23

9 REAL TIME COMPUTER

9.1 Control law and smart algorithms

For the SCAO module, we plan to use as a control law a classical integrator, with a modal control, together with a Kalman filtering for the windshake compensation. Hence the complexity of the RTC on this side should be limited.

We contemplate also to implement smart algorithms for the centre of gravity computation, either using a weighted centre of gravity method or centroiding by pixel selection. In the latter case, the centre of gravity is computed by taking into account only a given number of the brightest pixels. This method has been developed at Observatoire de Paris by E. Gendron and, being routinely used on the SESAME bench, has demonstrated its efficiency and robustness in the centre of gravity computation: it does not depend on the flux level, which may vary at each frame, it does not depend on the seeing and it prevents one from “dark frames” problem encountered in classical thresholding when all pixels are below the threshold. In addition, its algorithm is fast to execute.

9.2 Interfaces with telescope

The constraints (such as latency, type of date, etc) due to the necessary interaction between the RTC and the telescope should be accounted for when designing the RTC:

- the RTC commands will be sent to M4/M5,
- the RTC will need from the telescope some windshake information

10 PERFORMANCES

10.1 Atmospheric parameters

The atmospheric parameters adopted for deriving the SAMI performances are extracted from AD6, in particular from its Section 4.2, and are summarized in the following table.

	Value
Turbulence case	Median
Seeing @ zenith & 0.5 μm	0.65"
Zenith angle	30°
Outer scale	25 m
v_{mean}	16.4 m/s
h_{mean}	4007 m

Table 15: Turbulence model parameters

Given the 30° zenith angle, the actual seeing is 0.71", corresponding to r_0(0.5 μm)=14.5 cm.

10.2 Error budget decomposition

We explicit and comment hereafter the different terms of the global error budget:

$$\sigma^2_{tot} = \sigma^2_{fitting} + \sigma^2_{diff\,ref} + \sigma^2_{chrom} + \sigma^2_{aliasing} + \sigma^2_{temporal} + \sigma^2_{noise} + \sigma^2_{DM\,sat} + \sigma^2_{calib} + \sigma^2_{NCPA} + \sigma^2_{aniso}$$

- $\sigma^2_{fitting}$ corresponds to the ability of the deformable mirror to "fit" the turbulence and to the residual cophasing error of the M1 individual mirrors,
- $\sigma^2_{diff\ ref}$ corresponds to the error resulting in sensing the wavefront at a wavelength different from the imaging wavelength: due to differential refraction the wavefront sensor source does not appear at the same location on sky at these two wavelengths,
- σ^2_{chrom} corresponds to the error resulting in correcting a wavefront at wavelength different from the imaging wavelength,
- $\sigma^2_{aliasing}$ corresponds to high order aberrations un-measured by the WFS and seen as low order aberrations by the WFS,
- $\sigma^2_{temporal}$ corresponds to the error made in correcting an aberration measured some time before,
- σ^2_{noise} corresponds to the classical noise error but includes the effect of windshake…
- σ^2_{aniso} corresponds, when applicable, to the error made when the reference source and the science target at distant one from the other,
- $\sigma^2_{DM\ sat}+\sigma^2_{calib}+\sigma^2_{NCPA}$: in Phase A, these errors terms are not specifically analysed and we allocate for them a provision of 80 nm rms, corresponding to SR=95% in the K-band.

10.3 Fitting error

10.3.1 Turbulence term

We will use the M4 mirror of the E-ELT for correcting the wavefront errors. From AD7, the fitting error due to turbulence, in nm, is given by:

$$\sigma_{fitting} = 166 \times seeing^{5/6}$$

where *seeing* is given in arcsec. Hence, for a seeing of 0.65" at 30° zenith angle, one derives $\sigma_{fitting}$=125 nm rms.

Equalizing this equation with the following one:

$$\sigma^2_{fitting} = 0.257\, J^{-5/6} \left(\frac{D}{r_0}\right)^{5/3}$$

where $\sigma_{fitting}$ is in radians, one finds the equivalent number *J* of corrected Zernike modes: 5562.

10.3.2 M1 cophasing error

Little is still know about this error. We assume for this term an error of 50 nm rms.

10.4 Differential refraction error

Due to the differential refraction of the atmosphere with respect to the wavelength, resulting from the refraction index dependency with the wavelength, the apparent location on sky of the WFS reference source is different at the WFS wavelength and the imaging wavelength. It can be seen as an anisoplanatism error, with an anisoplanatism angle corresponding the angular distance between the WFS reference source locations at the two wavelengths.

$\theta_{diff\ ref}$ is this angular separation at a zenith angle of 30°, for the reference source at a WFS wavelength of 0.589 µm and an imaging wavelength of 2.2 µm. From the formulae in Section 5.4.3.1, one compute $\theta_{diff\ ref}$=0.37". The corresponding error $\sigma_{diff\ ref}$ for a 0.71" seeing and L_0=25m is 10 nm rms, computed thanks to the Chassat (1992) formulae (cf. also Section 10.8).

10.5 Chromatism error

From ATLAS Phase A study (AD9), for a 0.71" seeing, an outer scale of 25 m, a WFS wavelength of 0.589 µm and an imaging wavelength of 2.2 µm, this error is 25 nm rms.

10.6 Aliasing error

We consider the aliasing error to be 35% of the fitting error.

10.7 Temporal and noise errors

10.7.1 Simulation software

These errors are estimated in two steps, with two home-made simulation tools. The first one is an end-to-end simulation tool of an AO loop for a single Shack-Hartmann subaperture. It allows one to compute the noise error seen by a subaperture, given classical AO simulation parameters (Shack-Hartmann geometry, reference source flux, WFS transmission, detector

quantum efficiency and readout noise, sky flux, seeing, mean wind speed, WFS wavelength, loop frequency). The second tool allows one to compute the noise and temporal errors for the entire Shack-Hartmann given the noise error for a single subaperture, the r_0, L_0 and mean wind speed values, the loop frequency, the number of mirror actuators. This estimation can be made taking into account the windshake residuals by the implementation of a simple Kalman filtering. We describe with more details these two pieces of software in the following.

10.7.1.1 Single subaperture simulation

The goal of this simulation tool is to derive the noise level of the wavefront sensor, in terms of the different parameters of the Hartmann, namely:

- number of photons per frame
- WFS wavelength
- seeing
- subaperture diameter
- sampling frequency
- detector readout noise
- pixel size
- number of pixels
- centroiding method (either classical thresholded centre of gravity, or weighted centre of gravity, the latter one being actually used hereafter)
- loop local gain (equivalent loop gain between the subaperture and M4)
- wind speed

Our simulation tool simulates an unique subaperture of SAMI, on the E-ELT. The behaviour of the deformable mirror M4 is also simulated in front of this subaperture, with a local feedback loop with one frame delay. The program simulates a time-serie of Kolmogorov-like turbulent wavefronts. A high-resolution image of the spot at the focus of the micro-lens is computed, with its centre of gravity. This latter will be used as the reference for computing wave-front sensing errors.

The flux of the high-resolution image is then normalized, and the image resolution is then degraded to the resolution of the Shack-Hartmann wavefront sensor pixels, in order to form the wide pixels of the Hartmann. Some photon noise and read-out noise is added. On this Hartmann image, the centre of gravity is computed using

- a given number of different threshold values with thresholded centre of gravity
- another given number of different widths of weighting functions

Finally, the centroiding error is computed for each of the above values, and the minimum error (which allows one to optimize threshold value and width of weighting function) is searched for each simulation.

10.7.1.2 Simulation of an on-axis SCAO system for the E-ELT

We simulate SAMI as an AO system on Zernike polynomials, up to any arbitrary order (in our case n=84, i.e. J_{max}= 3655 modes).

10.7.1.2.1 Temporal PSD of the whole Zernike order

Assuming a Taylor' hypothesis, the PSD of a given Zernike mode *j* is given in the literature by

$$W_j(\nu) = \int_{-\infty}^{+\infty} \mid Q_j(\nu/V, y) \mid^2 \left((\nu/V)^2 + y^2 + 1/L_0^2\right)^{-11/6} dy$$

where $Q_j(x,y)$ is the Fourier transform of the mode $Z_j(x,y)$. Having obtained an analytical expression of

$$\sum_{j \in \, radial \; order} \mid Q_j(\nu/V, y) \mid^2$$

we can compute the sum of the PSD of the whole Zernike order, taking the outer scale effects into account.

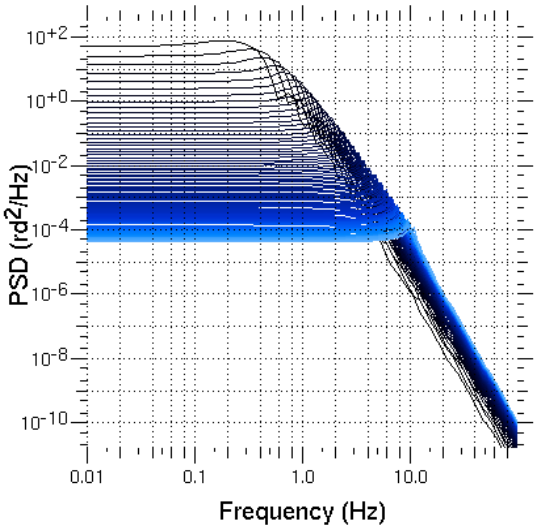

Figure 25: Example of the simulated Zernike spectra, cumulated over the whole radial orders, for D=42m and L_0=25m, for n=1 to 84 (the whole computation for the 84 orders takes 5.3 seconds).

10.7.1.2.2 Temporal error, noise error, and modal optimization

For each radial order, we compute the real transfer function of an AO loop, with any arbitrary loop delay (for the present study we took 1 frame delay) and integrator gain.

We assume that this transfer function is the same for any Zernike mode of the whole radial order, so that we can compute the temporal residual error of the whole order by integrating over frequencies the product between this transfer function by the cumulated PSD of all the Zernike modes of the considered order.

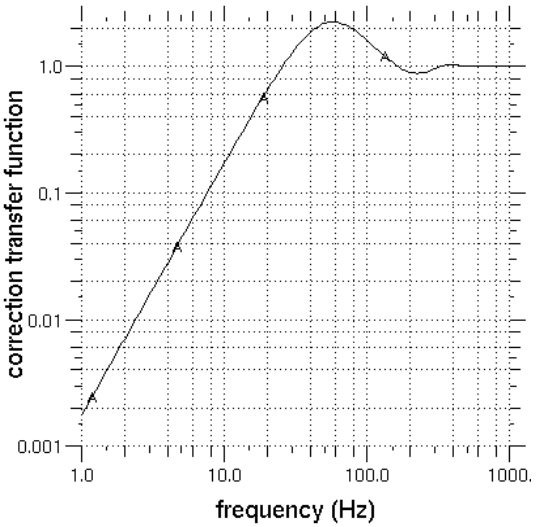

Figure 26: Example of the simulated loop transfer function for 500Hz sampling frequency and 2ms delay, with an integrator gain of 0.3.

From our single aperture simulation (cf. Section 10.7.1) we know, as an input, the noise variance at the sub-aperture level. We propagate spatially this noise onto the Zernike assuming a law in $\sigma_j^2 = 0.3\frac{\sigma_\varphi^2}{(n+1)^2}$ for each Zernike mode, which leads to the expression of the variance σ_n^2 for the full radial order:

$$\sigma_n^2 = 0.3\frac{\sigma_\varphi^2}{n+1}$$

We then know the level of the noise PSD and are hence able to deduce the noise variance that is propagated into the loop through the transfer function (from an analytical formula). This computation is done for any loop gain from 0 to 0.7 and we select the gain that led to the best performance, i.e. the best compromise between the noise error, increasing with gain, and the temporal error, decreasing with gain: this is a modal optimization.

As a by-product of this process, we can derive:

- the temporal error
- the noise error
- the optimum system bandwidth for each radial order
- the efficiency of the compensation for each radial order

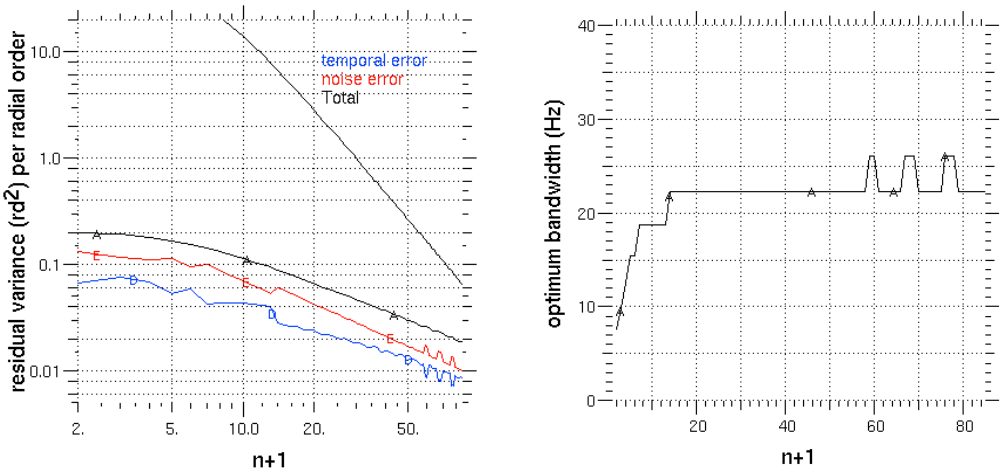

Figure 27: Example of the residual error (temporal and noise, on the left ; the upper black curve is uncorrected Zernike variance) and the optimum bandwidth (right) for r0=15cm, D=42, L0=25m and 330nm rms input WFS noise

10.7.1.2.3 Windshake compensation

Tip-tilt has a special treatment: we add the windshake PSD to the atmospheric PSD.

We use an analytical formula that fits the windshake PSD, and we simulate the temporal compensation that could be done by an advanced temporal compensator (such a Kalman filter of an high order). The transfer function of this filter is not modelled very accurately, but with a level of detail suitable for a phase A study only. While a pure integrator would have only a ν^2 law attenuation, the chosen model follows a ν^4 law at low frequency:

$$| H_{cor}(\nu) |^2 = \begin{cases} \nu^4/BP^4 & \nu < BP \\ 1 & \nu > BP \end{cases}$$

We compute the propagated noise and perform a modal optimisation with this filter exactly as described in the previous section. We treat the radial order n=1 (i.e. tip/tilt) as a whole and do not process tip in a different way than tilt. However, X and Y windshake properties are not the same and we should probably investigate a way to optimize this more finely during phase B.

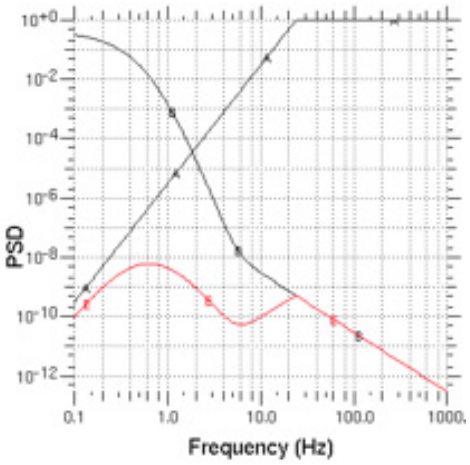

Figure 28: Example of the fitted windshake PSD (in arcsec^2/Hz), the modeled transfer function (with a bandpass of 25 Hz), and the product of both (in red).

10.7.2 Simulation results

Simulations are run assuming:

- V-band zero point: 1×10^{11} photons/s/m^2/μm
- Spectral bandpass: 0.35 microns (0.45-0.8 microns)
- Optical transmission: 0.546 (telescope: 65%, WFS: 84%)
- Detector quantum efficiency: 80%
- No sky background
- WFS wavelength: 0.6 microns
- Zenith angle: 30°
- r_0 at zenith and 0.5 microns: 15.9 cm (i.e. 14.5 cm at 30° zenith angle)
- L_0 at 0.5 microns: 25 m
- Mean wind speed: 16.4 m/s
- Number of subapertures: 84
- Maximum Zernike radial order considered: 84
- Detector readout noise: 3e- rms
- 1 frame delay
- Windshake residual PSD from ESO fitted according to the following figure (corresponding to 0.28 arcsec rms residuals)

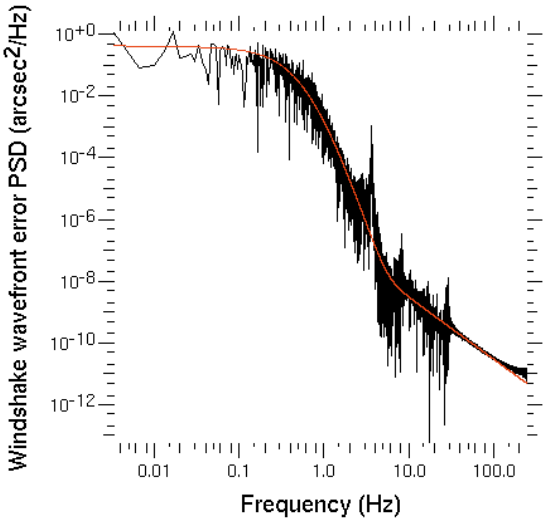

Figure 29: Windshake wavefront error PSD in arcsec^2/Hz and its fitted values in red

In all the following tables 16 to 20, large and aberrant temporal+noise error values should considered as real error values: they just mean that the loop cannot be closed for the corresponding configurations.

10.7.2.1 m_V=12

	2	4	6	8
1	461 347 237 226 364 323	350 168 125 115 108 121	342 156 105 106 96 112	341 157 107 98 102 101
2	364 201 140 123 116 113	343 159 103 95 89 94	343 159 105 94 89 82	344 159 106 89 94 93
3	352 170 114 107 96 84	346 164 105 92 82 91	346 163 107 94 87 83	347 166 105 90 92 87
4	349 166 104 84 85 82	349 163 103 94 85 85	348 165 103 91 84 83	350 169 108 93 86 92
5	348 160 97 86 84 78	350 160 100 89 81 81	350 162 104 95 85 87	350 162 97 91 89 86
6	350 161 95 86 80	349 162 102 88 82	350 166 100 95 84	350 162 105 84 86

	80	88	90	91
7	349 160 98 87 79 78	350 159 100 86 86 83	349 161 100 93 87 84	348 163 100 91 87 89
8	349 160 102 80 82 84	350 166 100 84 90 81	350 166 101 93 81 85	350 167 106 101 96 87

Table 16: Temporal plus noise error, in nm rms, for mV=12. Column values are for the number of pixels per subpupil and line values are for the pixel field of view, in units of $\lambda_{WFS}/d_{subpupil}$=0.25". In each box are given the errors for a loop frequency of 100, 200, 400, 600, 800 and 1000 Hz

10.7.2.2 m_V=13

	2	4	6	8
1	472 442 568 562 397 1727	356 195 186 163 205 214	346 180 156 152 176 189	345 177 158 162 186 196
2	368 210 167 153 138 172	347 173 133 128 129 140	347 178 133 130 138 148	347 175 135 143 146 148
3	357 182 137 124 132 132	350 173 125 127 132 132	350 171 129 124 134 132	351 173 126 125 128 146
4	351	349	352	352

	173 123 115 125 123	173 119 125 128 127	172 124 119 124 134	177 128 123 129 139
5	350 170 124 122 125 115	350 168 125 120 119 127	352 175 129 126 124 136	353 169 127 119 129 131
6	351 172 122 122 123 128	351 167 122 118 131 123	351 168 126 125 126 130	351 175 125 123 129 129
7	350 169 120 122 116 125	350 169 122 117 132 129	352 174 118 122 130 133	352 174 132 121 124 127
8	349 168 115 113 118 126	352 173 130 129 128 132	353 174 133 122 123 132	353 174 121 123 127 122

Table 17: Temporal plus noise error, in nm rms, for mV=13. Column values are for the number of pixels per subpupil and line values are for the pixel field of view, in units of $\lambda_{WFS}/d_{subpupil}$=0.25". In each box are given the errors for a loop frequency of 100, 200, 400, 600, 800 and 1000 Hz

10.7.2.3 m_V=14

	2	4	6	8
1	691 1116 944	383 288 291	365 253 328	364 259 317

	5941 1142 4638	406 428 477	372 360 491	362 460 463
2	372 253 254 302 382 7409	358 210 209 239 295 356	358 222 222 268 318 415	358 223 238 303 345 393
3	360 212 196 222 247 269	357 207 189 213 275 313	358 208 206 228 247 355	359 215 219 280 312 413
4	358 195 184 193 236 257	358 194 190 225 256 359	357 197 192 244 260 325	358 206 198 219 300 354
5	358 193 191 207 275 274	356 199 196 209 291 328	356 204 195 232 442 338	357 202 197 242 556 1316
6	356 195 181 202 1830 548	357 199 187 246 457 7137	359 204 196 203 328 391	358 202 188 219 260 6650
7	356 197 182 203	355 198 201 243	358 197 185 266	358 206 182 279

	236 291	445 2917	12190 12546	464 15325
8	356 196 178 184 255 241	358 206 201 276 456 2710	357 201 196 481 10616 10293	358 203 194 228 348 4665

Table 18: Temporal plus noise error, in nm rms, for mV=14. Column values are for the number of pixels per subpupil and line values are for the pixel field of view, in units of $\lambda_{WFS}/d_{subpupil}$=0.25". In each box are given the errors for a loop frequency of 100, 200, 400, 600, 800 and 1000 Hz

10.7.2.4 m_V=15

	2	4	6	8
1	3249 1955 3616 4720 3483 1896	513 497 716 1697 2280 1480	455 519 685 1099 935 908	459 497 667 925 735 881
2	431 405 1080 608 3437 9664	395 353 581 771 762 821	402 387 543 729 860 785	402 397 550 947 792 1122
3	389 321 328 10020 6880 7657	385 311 458 550 694 1209	393 351 488 735 1198 1334	397 356 511 816 1296 1199
4	377 289 393 9706 15331 7103	390 311 398 598 808 4256	386 307 708 7245 4929 8215	386 334 494 1414 2759 9238

5	380 285 1719 1845 15331 10140	386 305 493 5665 988 6560	387 294 15331 10870 8831 15299	385 308 1560 15331 11085 6339
6	378 284 15331 5231 13584 4799	380 287 7213 9013 9158 15331	384 322 2009 8050 8381 10621	386 314 10874 12390 11979 8142
7	384 286 342 593 13798 5810	376 284 10749 13969 15331 3316	380 297 15331 7464 12863 13025	385 305 8502 15331 15331 15331
8	377 288 344 12515 7512 719	380 304 14777 7719 15331 10120	385 279 551 15331 14061 15331	382 293 709 13175 15331 15331

Table 19: Temporal plus noise error, in nm rms, for mV=15. Column values are for the number of pixels per subpupil and line values are for the pixel field of view, in units of $\lambda_{WFS}/d_{subpupil}$=0.25". In each box are given the errors for a loop frequency of 100, 200, 400, 600, 800 and 1000 Hz

10.7.2.5 m_V=16

	2	4	6	8
1	15331 15331 15331 7495 5824 10080	735 1062 1616 1464 2142 1702	754 902 1075 1206 1302 1555	825 1027 1326 1028 1864 1557
2	660 15272	597 807	628 794	630 864

	15331	1115	1262	1402
	2814	1073	1738	1749
	9421	1671	1441	2068
	2746	1270	1570	1424
3	507	525	548	593
	14567	769	798	797
	8859	1542	1350	1241
	15331	2078	1233	4969
	11106	1980	1880	3248
	8727	2131	2113	2246
4	505	510	509	526
	12779	665	8880	716
	10793	3336	3433	1820
	6878	5974	6086	9038
	15331	10085	7451	11001
	15213	7493	7104	15331
5	489	521	621	511
	15331	997	8722	1196
	15331	13614	2407	14070
	13516	7297	5780	10556
	11130	15331	15331	15331
	12608	9116	11600	9762
6	487	496	519	529
	15331	5742	1750	15331
	15331	14598	15331	15331
	14516	14927	15311	15331
	6422	15331	15331	12357
	15331	15331	15331	12988
7	495	553	623	536
	659	1019	15331	15331
	15331	15331	15331	15331
	12065	15331	15331	11764
	15331	13529	15331	11775
	15331	7046	10342	12088
8	497	767	1467	573
	11895	15331	15331	2769
	15331	15331	15331	8314

	15331 1447 13502	12398 13779 15149	15331 15331 15331	15331 15331 15331

Table 20: Temporal plus noise error, in nm rms, for mV=16. Column values are for the number of pixels per subpupil and line values are for the pixel field of view, in units of $\lambda_{WFS}/d_{subpupil}$=0.25". In each box are given the errors for a loop frequency of 100, 200, 400, 600, 800 and 1000 Hz

10.7.3 First conclusions

If the four-quadrant configuration (2×2 pixels/subaperture) almost always gives the lowest noise, other numbers of pixels per subaperture lead to similar values. Given the specific issues of gain calibration of a four-quadrant configuration, one could then favour a 4×4 configuration.

Concerning the pixel field of view, large values (~5-6×λ_{WFS}/d_{subap}~1.24"-1.49") lead to the lowest noise.

10.8 Anisoplanatism error

This error contribution is estimated using the Chassat (1992) formulae. They allow one to analytically compute the anisoplanatism phase error given a turbulence model. Results, using the numbers of Section 10.1 and the atmospheric model of AD6, are given in the following table.

Distance from reference source (arcsec)	Anisoplanatism error for L_0=25m (nm rms)	Corresponding Strehl loss at 2.2 microns
5	101	92%
10	184	76%
15	253	59%
20	305	47%
25	354	36%
30	396	28%
35	433	22%
40	475	16%
45	518	11%
50	571	7%
55	554	8%
60	579	6%

Table 21: Anisoplanatism errors for a seeing of 0.71" and L_0=25 m

10.9 Error budget values

	m_V=12	m_V=13	m_V=14	m_V=15	m_V=16
Fitting error Turbulence term	125	125	125	125	125
Fitting error M1 cophasing	50	50	50	50	50
Differential refraction error	10	10	10	10	10
Chromastism error	25	25	25	25	25
Aliasing error	44	44	44	44	44
DM saturation, calibration and NCPA errors	80	80	80	80	80
Temporal and noise error	80	122	181	284	487
Total error	183	205	245	328	514
Corresponding Strehl	76%	71%	61%	41%	12%

Table 22: Error budget values, in nm rms and corresponding on-axis Strehl at 2.2 microns for different reference star magnitude

11 CALIBRATIONS

11.1 Reference slope calibrations

The measurement of the reference slopes will be performed thanks to a source positioned at the WFS field stop. The WFS will be moved (in X-Y) in front of this fibre-fed source for this measurement.

A special care will have to be taken to the accurate alignment of this fibre together with the optical axis of the WFS K-mirror. It could be achieved by checking that the beam is not deviated when rotating the K-mirror. An alternative could be to average out the reference slope measurements when rotating the K-mirror.

11.2 Interaction matrix

The measurement of the interaction matrix requires the use (and then the implementation) of a visible point-like source at the E-ELT intermediate focus, between M2 and M3.

In addition, this measurement requires delineating physically the pupil. We hence propose to use a pupil mask in front of the micro-lenses.

11.3 Non-common path aberrations

We propose to measure the non-common path aberrations thanks to a classical phase diversity method. It requires using (and then implementing) an infrared point-like source at the E-ELT intermediate focus. An alternative would be to proceed with the phase diversity on sky using a bright source.

11.4 Pupil monitoring

In our design, the pupil shifts are compensated by tilting the M11 mirror. It thus requires monitoring these pupil movements. Different solutions are conceivable for this monitoring:

- measure the illumination of the subpupils at the edge of the Shack-Hartmann. Though, since we contemplate to use a pupil mask in front of the micro-lenses to calibrate the interaction matrix, the pupil shifts would be inferred only from the lack of illumination of the subpupils at the edge, which is not as robust as inferring these pupil shifts also from the illumination of subpupils oustide the pupil.
- infer the pupil shifts from on-sky interaction matrix measurements. This method has been used by E. Gendron during NAOS AIT and is being simulated by H. Bonnet at ESO. Though, we fear that this method could be difficult to apply on faint sources.
- measure the pupil shifts using sources on M4 and dedicated (4-quadrants) detector(s) inside the WFS.

To our knowledge, none of these methods has been used in operation at telescope. Their feasibility and limitations will be studied in Phase B.

12 RISK ASSESSMENT

The main risks we have indentified are:

- the manufacturing of the dichroic plate, with the dimensions and assumptions used in this study: optical quality, transmission and reflection coefficients. A feasibility study will be done in Phase B.
- the ability to monitor the pupil shifts. No method has not been clearly identified yet. To mitigate the risk, one should consider implementing visible light-sources on M4. It would allow one to track the M4 position, which is not currently possible.
- the availability of WFS visible detectors, with the characteristics given in AD5.

13 INTERFACE REQUESTS

The main request we have identified concerns the calibrations of the SCAO module (cf. Section 11) and its RTC:

- a visible point-like source at the E-ELT interface focus between M2 and M3,
- an infrared point-like source at the E-ELT interface focus between M2 and M3,
- visible light sources on M4,
- availability of windshake data for the SCAO wavefront sensor.

14 CONCLUSION

This study has presented a possible implementation of an SCAO module for MICADO. If few points are still to be confirmed (e.g., the lack of need for an ADC) or investigated (e.g., the pupil movement monitoring), it showed that the MICADO top-level requirements could be fulfilled. First performance estimations, that have to be consolidated in Phase B, show that such an SCAO module could reach a ~75% Strehl ratio for an on-axis m_V=12 guide star.